High-resolution imaging of cellular dopamine efflux using a fluorescent nanosensor array

Sebastian Kruss[a,1], Daniel P. Salem[a], Lela Vuković[b,c,2], Barbara Lima[a], Emma Vander Ende[a], Edward S. Boyden[d,e], and Michael S. Strano[a,3]

[a]Department of Chemical Engineering, Massachusetts Institute of Technology, Cambridge, MA 02139; [b]Department of Physics, University of Illinois at Urbana–Champaign, Champaign, IL 61801; [c]Department of Chemistry, University of Texas at El Paso, El Paso, TX 79968; [d]Media Lab, Massachusetts Institute of Technology, Cambridge, MA 02139; and [e]McGovern Institute for Brain Research, Massachusetts Institute of Technology, Cambridge, MA 02139

Edited by David R. Walt, Tufts University, Medford, MA, and accepted by Editorial Board Member John A. Rogers January 11, 2017 (received for review August 23, 2016)

Intercellular communication via chemical signaling proceeds with both spatial and temporal components, but analytical tools, such as microfabricated electrodes, have been limited to just a few probes per cell. In this work, we use a nonphotobleaching fluorescent nanosensor array based on single-walled carbon nanotubes (SWCNTs) rendered selective to dopamine to study its release from PC12 neuroprogenitor cells at a resolution exceeding 20,000 sensors per cell. This allows the spatial and temporal dynamics of dopamine release, following K^+ stimulation, to be measured at exceedingly high resolution. We observe localized, unlabeled release sites of dopamine spanning 100 ms to seconds that correlate with protrusions but not predominately the positive curvature associated with the tips of cellular protrusions as intuitively expected. The results illustrate how directionality of chemical signaling is shaped by membrane morphology, and highlight the advantages of nanosensor arrays that can provide high spatial and temporal resolution of chemical signaling.

sensors | imaging | dopamine | carbon nanotubes | chemical signaling

Chemical signaling between cells is a hallmark of life, with one key example being neurotransmitter release from neurons to transmit and process information (1). However, unlike electrical potential, the measurement of chemical signaling between cells and within cellular networks is not as well developed, despite its importance to cellular biology. Neurotransmission via neurotransmitters, paracrine signaling between immune cells, or quorum sensing between bacteria in biofilms (2, 3) rely on spatial and temporal precision in chemical signaling. Analytical tools are not yet available to resolve these dynamics. Recently, the groups of Lindau and Ewing used 4–16 microelectrodes per array per chromaffin cell to estimate catecholamine release direction and dynamics (4–6). Nanosensors have several advantages for the study of cell signaling, as we have highlighted (7, 8). Their nanoscale size means that they can form dense arrays, increasing the number of probes per cell. In this work, we construct a fluorescent nanosensor array placed in the vicinity of PC12 neuroprogenitor cells at a density of ∼20,000 sensors per cell, with better than 100-ms temporal resolution to study dopamine release with much higher resolution.

The platform uses near-infrared (nIR) fluorescent single-walled carbon nanotubes (SWCNTs) rendered chemically selective to dopamine. nIR fluorescent single SWCNTs are versatile building blocks for biosensors and demonstrate detection limits down to single molecules (9–13). We selected the neurotransmitter dopamine for this study because of its central role for reward control and learning and because it is one of the neurotransmitters for which volume transmission is heavily discussed (14, 15). The spatially dependent concentration profile of dopamine plays an especially important role when neurotransmitters spill over from synapses and freely diffuse in all directions (volume transmission) through neural tissue (14, 16, 17). By placing such dopamine-sensitive nanosensors in arrays beneath dopaminergic cells we are able to image dopamine efflux, identify hotspots on the cell surface, and map the directionality of dopamine efflux (Fig. 1*A*). This platform has advantages over protein-based fluorescent sensors and semisynthetic protein–fluorophore conjugates on the cell surface in that it has higher sensitivity, time resolution, and lacks photobleaching (18–21). Electrochemical techniques, although the most advanced for measurement of redox-active neurotransmitters in vitro and in vivo, provide poor spatial resolution (4, 6) to date. Indirect (optical) methods can label cellular components that are involved in exocytosis or load vesicles with fluorescent dyes but cannot directly detect the molecules of interest or their dynamics in the extracellular space (22–24).

Results and Discussion

Previously we found that the corona phase around SWCNTs can be engineered to recognize certain small analytes—a phenomenon we termed Corona Phase Molecular Recognition (CoPhMoRe) (7, 25, 26). Specifically, DNA-wrapped SWCNTs were found to increase their nIR fluorescence in the presence of catecholamines (13). Here, we synthesized and characterized different DNA/SWCNT complexes and identified the best candidates for dopamine detection (*SI Appendix*, Fig. S1). We measured the fluorescence responses of a panel of 10 DNA-wrapped (6, 5)-chirality enriched SWCNTs versus a panel of 15 molecules (*SI Appendix*, Figs. S2–S4) including dopamine, dopamine homologs, and potential interfering compounds present in biological environments (*SI Appendix*, Fig. S2). Our results

Significance

Cells communicate between themselves using waves of chemical concentration that change in both direction and time. Existing methods are not able to capture this spatial and temporal dependence at the necessary resolution to study the influence of cellular morphology. This study utilizes arrays of fluorescent nanosensors based on single-walled carbon nanotubes placed under and around neuroprogenitor cells to label-free image the efflux of the neurotransmitter dopamine. We use the spatiotemporal resolution of this approach to resolve where on the cell surface dopamine is released and how cell morphology affects the location of release sites.

Author contributions: S.K., E.S.B., and M.S.S. designed research; S.K., D.P.S., L.V., B.L., and E.V.E. performed research; S.K., D.P.S., L.V., and M.S.S. analyzed data; and S.K., D.P.S., and M.S.S. wrote the paper.

The authors declare no conflict of interest.

This article is a PNAS Direct Submission. D.R.W. is a Guest Editor invited by the Editorial Board.

[1]Present address: Department of Chemistry, Institute of Physical Chemistry, Göttingen University & Center for Nanoscale Microscopy and Molecular Physiology of the Brain, 37077 Goettingen, Germany.

[2]Present address: Department of Chemistry, University of Texas at El Paso, El Paso, TX 79968.

[3]To whom correspondence should be addressed. Email: strano@mit.edu.

This article contains supporting information online at www.pnas.org/lookup/suppl/doi:10.1073/pnas.1613541114/-/DCSupplemental.

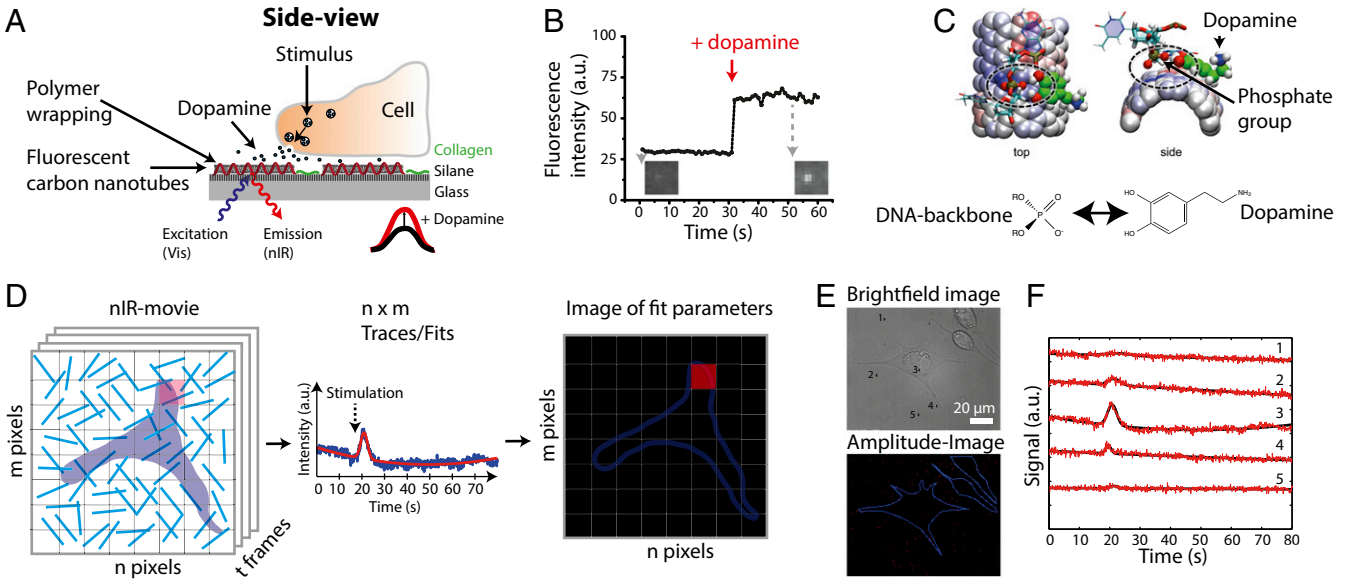

Fig. 1. Chemical imaging using nanosensor arrays. (*A*) Fluorescent carbon nanotubes are rendered sensitive to dopamine by noncovalently attaching specific DNA sequences to them. They are immobilized onto a glass substrate, and dopamine-releasing PC12 cells are cultivated on top. When cells are stimulated they release dopamine and the SWCNT fluorescence changes. (*B*) Fluorescence intensity trace of a single $(GA)_{15}$-ssDNA/SWCNT imaged on a surface while adding dopamine (10 µM). (*C*) Proposed sensing mechanism: Dopamine pulls phosphate groups to the SWCNT surface, which removes quenching sites and increases SWCNT fluorescence quantum yield (MD simulations). (*D*) PC12 cells are cultivated on top of a substrate coated with nanosensors. In an image of this substrate every pixel corresponds to a region containing one or more nanosensors and serves as a reporter of local dopamine concentration. Each pixel of an nIR-movie produces a trace that contains information about the dopamine signal. A fitting procedure of every trace yields amplitude, width, and time point of the signal. Those values can be represented in false-color images, and their spatial composition can be further analyzed. (*E*) Bright-field image of a PC12 cell adhering on top of a nanosensor array and corresponding image of signal amplitudes. (*F*) Examples for pixel traces from regions under and around the cell shown in *E*.

indicate that $(GA)_{15}$-ssDNA/SWCNT complexes provide the most promising selectivity and sensitivity profile for cell experiments (Fig. 1*B* and *SI Appendix*, Figs. S4–S6). These dopamine nanosensors were excited with a laser at 560 nm in a standard fluorescence microscope equipped with an nIR-camera that detects the nIR emission of (6, 5)-SWCNTs at ∼980 nm. We performed molecular dynamics (MD) simulations to gain a deeper understanding of molecular recognition of these sensors. Our results show that dopamine interacts via its two hydroxy groups with phosphate groups of the DNA backbone (Fig. 1*C*). This interaction pulls the phosphate group closer to the surface of the SWCNTs and changes the local potential (*SI Appendix*, Figs. S21–S26). These findings rationalize previous phenomenological theories of molecular recognition in the corona phase of SWCNTs (27, 28). Furthermore, we found that naked SWCNTs do not respond to dopamine at all (*SI Appendix*, Fig. S8 and S10) and the least responsive DNA sequences showed the highest (starting) fluorescence counts (*SI Appendix*, Figs. S9–S11). This result suggests that movement of the phosphate groups removes (pre)-quenching sites for excitons and that dopamine's ability to pull these groups to the SWCNT surface results in an increase of SWCNT fluorescence.

With respect to the envisioned application (Fig. 1*A*) we prepared homogeneously coated nanosensor surfaces and treated every pixel of the nIR image as a local sensor. Whereas nanosensors are randomly adsorbed on the surface, it would be possible to pattern them more regularly as it was shown for other nanoparticles (29–31). The SWCNT sensors were densely coated on the surface to maximize the signal/noise ratio (*SI Appendix*, Figs. S12–S14). Ensemble calibration curves (*SI Appendix*, Fig. S5) indicate that we can detect dopamine concentrations down to 100 nM (*SI Appendix*, Fig. S5). However, this is the mean response of a large population of sensors. When we analyzed individual nanosensors in the single-molecule regime (100 pM) we observed stochasticity indicative of binding and unbinding events of single dopamine molecules (*SI Appendix*, Fig. S7). To ensure that our sensors were capable of detecting dopamine in the presence of cells, we cultivated dopamine-releasing pheochromocytoma cells (PC12) on top of nanosensor arrays that were additionally coated with collagen to increase cell adhesion (*SI Appendix*, Figs. S13–S16). Collagen has been known to increase PC12 cell adhesion and differentiation, whereas nanotubes affect neurite outgrowth (32–35). Furthermore, the elasticity of the substrate affects PC12 cell morphology (36). PC12 cells on our sensor/collagen-coated surfaces attained a morphology similar to PC12 cells cultured without sensors. Similar scenarios in the literature are nanotube networks that were glycosylated to enhance biocompatibility and have been used for amperometric studies of dopamine release (37). This procedure increased adhesion and viability of PC12 cells on SWCNT networks. We focused our investigation mostly on isolated PC12 cells and not clusters to minimize cross-talk from different cells.

Labeling with the fluorescent false neurotransmitter FFN551 showed that PC12 cells on these surfaces contain vesicles with dopamine transporters, indicating dopamine-containing vesicles (*SI Appendix*, Fig. S16) (24, 38). After 1 d of cultivation at 37 °C in full culture medium, the medium was exchanged to PBS buffer and the response to dopamine and homologs (10 µM) was tested. The results (*SI Appendix*, Fig. S6) show that the nanosensor arrays are still functional and resist biofouling. Catecholamine homologs such as epinephrine, norepinephrine, and ascorbic acid could interfere with this array (*SI Appendix*, Fig. S6). Therefore, the sensor array reports about the total changes in the concentration of all catecholamines (ascorbic acid concentrations should be negligible/constant). However, PC12 cells are thought to mainly release dopamine even though pharmaceuticals and hypoxia can affect the ratio between the different catecholamine neurotransmitters (32, 39, 40). Consequently, sensor responses are expected to be attributed mainly to dopamine and to a lesser extent other catecholamines.

The results from Fig. 1 indicate that we can use surface-immobilized nanosensors to optically detect dopamine in the presence of PC12 cells. Consequently, we recorded nIR movies (100 ms per image, 640 × 512-pixel resolution, 212 nm/pixel) of PC12 cells adhered on collagen-coated nanosensor arrays and stimulated the cells with potassium buffer to observe dopamine release. To increase the signal to noise ratio, we divided the field of view into squares of 4 × 4 pixels and developed a fitting algorithm for the normalized intensity traces of the pixel groups. This algorithm fits the curve $f(t) = a + bt + ct^2 + xe^{-((t-y)^2/2z^2)}$ to the intensity traces (Gaussian function plus background correction; Fig. 1 *D–F*).

Consequently we get 20,480 "reporter" pixels per fitted image (pixel size ~850 × 850 nm). Therefore, we expect ~1,700 reporter pixels under a (round) cell (d = 40 μm), >180 reporter pixels in a 2-μm zone around the cell, and ~150 reporter pixels under the cell contour (pixel size = 850 × 850 nm). The fitting process reduced the 3D movie to a 2D image of fitting parameters, which can then be further analyzed (Fig. 1*D*). The different fitting parameters represent how the local reporter pixel responds to dopamine and the parameters account for amplitude (x), width (y), and time point (z) of the event. Fig. 1*F* shows typical traces from different locations under the cell, from the cell border, and other regions [1–5, shown in the bright-field (BF) image of Fig. 1*E*].

We performed independent analyses to verify that (*i*) temporal and (*ii*) spatial patterns are related to the stimulation time point and the location of cells. To verify the temporal correlation in raw data traces (Fig. 2*A*), we defined three periods (before, during, and after stimulation) and searched for maxima (in each period) that would indicate a dopamine-induced fluorescence increase. The exact stimulation time point (±1 s) was known from the time point when K^+ was added on top of the cells. The nonrandom distribution during the stimulation period proves that the observed sensor responses are related to stimulation (Fig. 2 *A* and *B*).

Histograms of the normalized sensor signals from different regions of interest related to the cell (shown in white in Fig. 2*C*, *Left*) prove that the signals are not randomly distributed throughout the image. Specifically, there is a clear spatial correlation between responses (normalized amplitude change) and regions associated with the cell (e.g., cell border, cell body). The time resolution of our approach (100 ms) is not yet fine enough to observe a propagating wave of dopamine released by the cell given that the diffusion length scale during image acquisition $x = \sqrt{2Dt}$ is ~12 μm [$D = 7.63 \times 10^{-6}$ cm^2/s (14)], comparable to the cell diameter. However, the technique is able to localize release events and their duration as shown below.

Fig. 3*A* shows the fitted response of the sensors at different time points from the contour of a single cell (shown in Fig. 3*B*, *Left*). The 3D plots show the sensors turn on after cell stimulation, which indicates release of dopamine. Furthermore, the responses decay as dopamine unbinds and diffuses away. Fig. 3 *B–E* shows bright-field images of four different cells and corresponding 3D plots of the sensor response magnitudes along the cell contour (line width = 850 nm). Here, in contrast to the time-resolved Fig. 3*A*, the maximum responses of the whole experiment are shown (fit parameter x). The height and color of the 3D plots indicate the magnitude of sensor responses indicative of higher transient dopamine concentrations (Fig. 1*D*). For clarity we only show responses along this contour (full response plots are shown in *SI Appendix*, Fig. S17 and a time-resolved full hotspot analysis in *SI Appendix*, Fig. S18).

The contour is also the most interesting region because efflux parallel to the nanosensor array is centered there with dopamine concentrations highest at exocytosis sites. The response profiles show heterogeneity along the contour, which is expected from multiple dopamine release sites. Furthermore the shape of the cell affects the distribution of release sites. Fig. 3 demonstrates the superior spatial resolution of our sensing strategy compared with existing technology. For example, the groups of Lindau and Ewing used microelectrode arrays with up to 4–16 electrodes (per cell) to "image" catecholamine release from chromaffine cells (4–6). In contrast, our approach contains 349, 242, 192, and 206 sensor pixels just along the contour of the four cells shown in

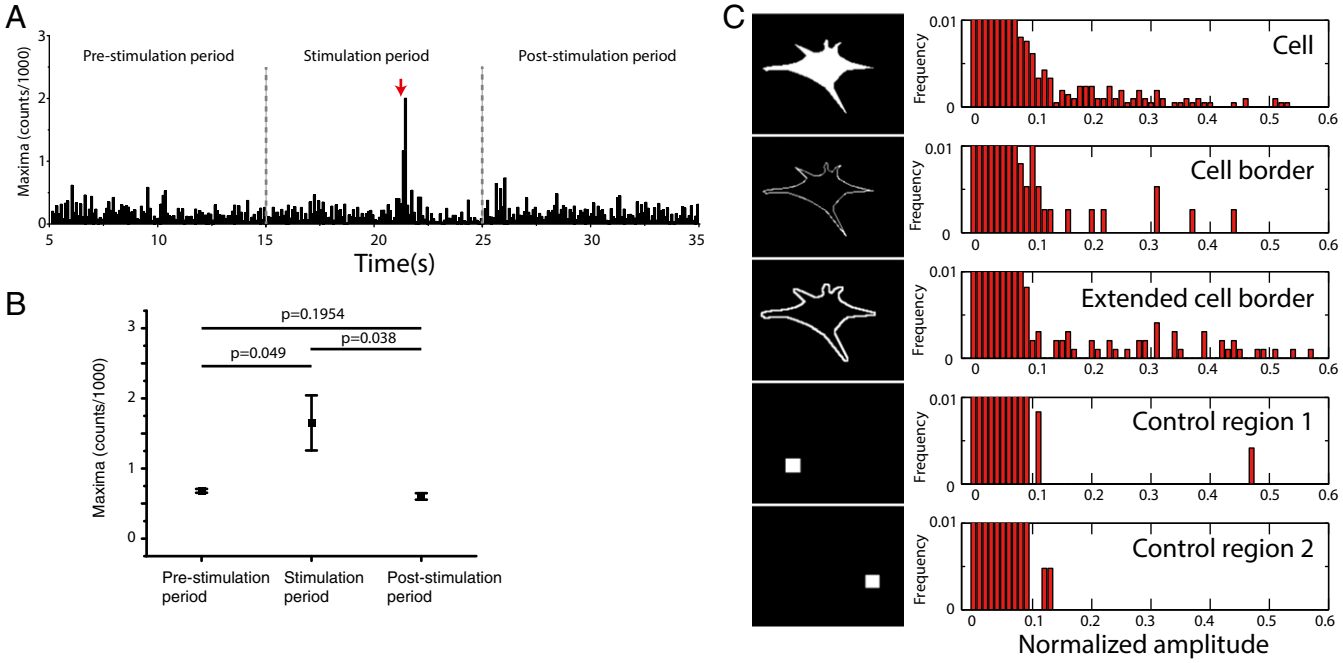

Fig. 2. Spatial and temporal correlation between sensor response and cells. (*A*) Temporal correlation between stimulation event and sensor responses (single experiment). (*B*) Large amplitudes are more likely in time intervals with cell stimulation. Two-sided t test of independent experiments (n = 4). (*C*) Spatial correlation between sensor responses (normalized amplitude change) and parts of the cell. The black/white image on the left indicates the regions/pixels (in white) that were analyzed. The histograms show that the sensor responses are related to the cell and are not randomly distributed.

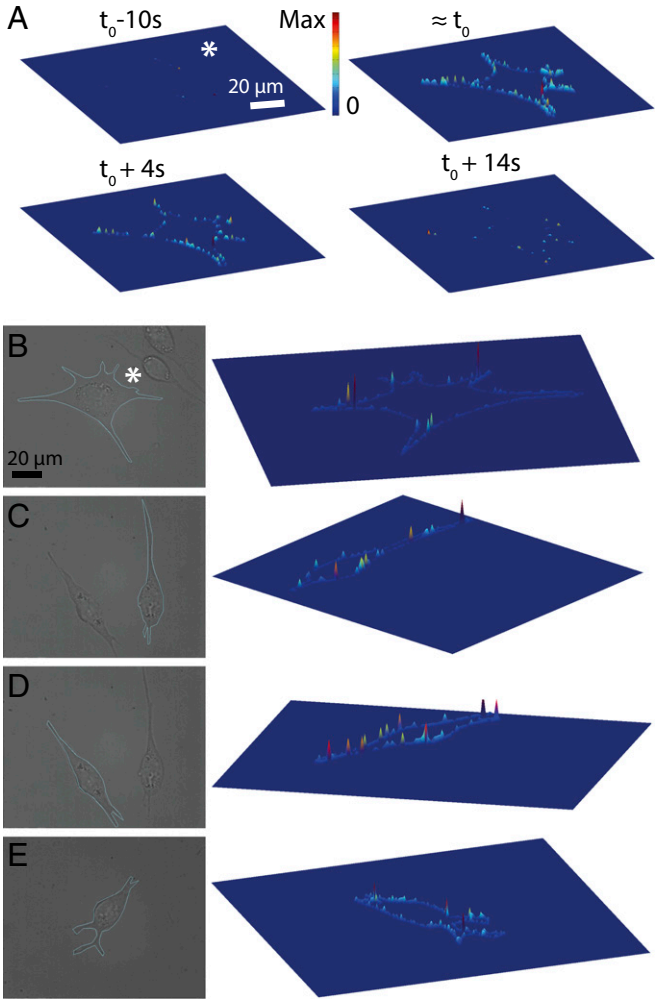

Fig. 3. Dopamine release profiles along the cell border. (*A*) Three-dimensional plots of fitted sensor responses along the cell border at different time points relative to the stimulation at t_0 (the corresponding cell is shown in *B*). Height and color indicate the relative fluorescence change normalized to the maximum fluorescence change of the experiment. Other areas are shown in blue for clarity. (*B–E*, *Left*) Bright-field image of PC12 cells adhering on top of collagen-coated dopamine nanosensor arrays (contour shown in light blue). (*Right*) Three-dimensional plot of maximum sensor responses (of all frames) along cell contour. Height and color indicate magnitude of the dopamine response, which correlates with dopamine concentration. Other areas are shown in blue for clarity.

Fig. 3 *B–E* and even more (>20,000) in the vicinity of the cell. Therefore, with nanosensor arrays there are around two orders of magnitude more sensors positioned on the contour of a single cell and more than three orders of magnitude more sensors in the area close to the cell. Compared with amperometric methods, nanosensor arrays currently exhibit reduced temporal resolution but amperometric methods cannot distinguish molecules of similar redox potential. Therefore, due to the higher chemical selectivity it is more appropriate to compare nanosensor arrays with cyclic voltammetry methods, which also have a time resolution of ∼100 ms (20). An advantage of amperometric methods is their ability to quantify (count) the number of molecules that encounter the electrode. Fluorescent sensors are more complex in terms of their signal transduction mechanism but are also capable of detecting single molecules (*SI Appendix*, Fig. S7) and could in principle be calibrated.

In a next step we further analyzed data such as those shown in Fig. 3 to answer longstanding questions about dopamine efflux from PC12 cells. If we focus on responses >3× of the mean response (along the cell contour) we can pinpoint to locations that we refer to as hotspots (>3× mean response) and are distinct from locations close to the noise level. Fig. 4 *A–C* shows line profiles of the sensor response along the cell contour. Hotspots are maxima in these line plots. They are also shown in the cell contour in Fig. 4 *A–C* as blue dashed circles. Arrows in both plots indicate locations on the cell surface and the line plots show the responses in a clockwise fashion. It is striking that not all cells show hotspots, which means that not every stimulation finally leads to dopamine release. This behavior is known for PC12 cells and ∼50% of stimulation events do not lead to dopamine release as measured with electrochemical methods (33).

Our results indicate 2–17 hotspots per cell (contour). This number is in agreement with electrochemical results from Zerby and Ewing that indicated ∼28 release events of PC12 cells per stimulation (41). Hotspots have been discussed in the past but the lack of spatial resolution of electrode-based methods made it impossible to directly pinpoint release sites on single cells (42). It is also known that neurons do not necessarily form well-defined synapses and therefore it is not known a priori where cells release signaling molecules (43).

Interestingly, hotspots are not accumulated at the tips of protrusions (see also Fig. 3). The local curvature of the cell outline was calculated and is color-coded in the cell contour plots in Fig. 4. Our data (Fig. 4*F*) indicate that more hotspots are found in regions of negative curvature (64%) compared with regions with positive curvature (36%).

However, 65% of the pixels along the cell contours ($n = 8$) have a curvature <0. The reason for this ratio is that cells with protrusions have many slightly concave segments and fewer strongly convex segments (tips). If the number of hotspots at a given curvature is normalized to the probability of this curvature (in all cells), there is no preference for either negative or positive curvature such as tips of protrusions (*SI Appendix*, Fig. S20). However, the nanosensor approach generates single-cell data about hotspot distribution (Figs. 3 and 4 *A–C*) and averaging might bury information.

Previously, it was shown that nondifferentiated PC12 cells release dopamine from the cell body, whereas differentiated PC12 cells release it mainly from structures called varicosities. However, our data indicate that they are distributed along cell protrusions with similar probabilities for regions of positive and negative curvature (41). Curvature and membrane tension are known to be a driving force of exocytosis and therefore spatially resolved images such as in Fig. 4 could provide new insights into this process (44).

Our analysis focused on the cell border because it is the most relevant region for studying signaling to other cells. Nevertheless, when all sensors under the cell are analyzed, hotspots under the cell appear (*SI Appendix*, Figs. S17 and S18). Total internal reflection fluorescence microscopy studies of labeled vesicles demonstrated exocytosis from the bottom of chromaffine cells (45). However, these methods naturally focus on the parts of the cell close to the substrate (i.e., cell bottom). Other studies with different techniques reported exocytosis from the whole cell surface (46, 47). Our data (Fig. 4 and *SI Appendix*, Fig. S17) show that there is release from regions close to the cell border but also from the cell bottom. It is possible that the functionalization of the substrate and cell adhesion affect the distribution of release sites. Furthermore, our sensors directly image the released molecule whereas these other optical methods image the membrane fusion process.

We further analyzed directionality of release. Fig. 4 *A–C* (*Right*) shows the signals from the cell perimeter region relative to center of mass of the cell and the arrow lengths indicate signal amplitudes. These plots reveal anisotropy of release—a measure not accessible with other methods. Anisotropy of cells translates into an anisotropy of dopamine release.

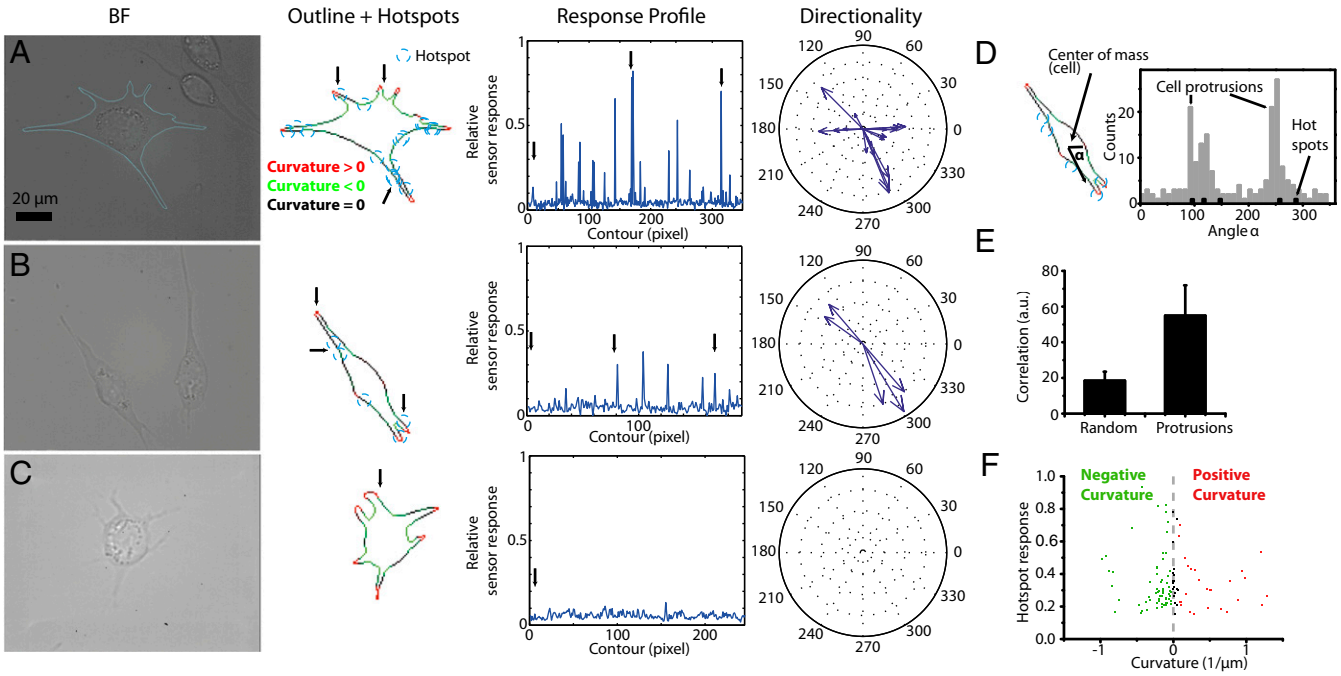

Fig. 4. Hotspots and directionality of dopamine release. (*A*–*C*) Bright-field (BF) images of PC12 cells cultivated and stimulated atop nanosensor arrays. Responses were analyzed along the contour of the cell (width ~850 nm) and show hotspots (defined as 3× the mean response). Blue circles indicate hotspots in the contour picture. Arrows point at specific locations of the cell and corresponding locations in the response profile along the cell contour. Directionality plots show angular distribution of hotspots. Length of arrows is proportional to the magnitude of the sensor response. (*D*) Anisotropy of dopamine release is governed by the distribution of protrusions/cell surface. The histogram shows the angular distribution of contour pixels (cell in *A*). Hotspots are shown in black and reveal that they are correlated with protrusions (shown in grey). (*E*) Hotspots are not randomly distributed but colocalize with protrusions ($n = 8$). Errors are SEMs. (*F*) Hotspot magnitudes (from $n = 8$ cells) versus local curvature. Hotspots are more often found in regions of negative curvature (64% vs. 36%) but due to cell morphology there is also more negative curvature per cell (see *SI Appendix*, Fig. S20 for normalized histograms).

The most important cell features that govern anisotropy are protrusions. Hotspots are associated with protrusions (Fig. 4 *D* and *E*)—not necessarily at the tips but as well in regions where the protrusions begin (corresponding to negative curvature). To calculate a correlation, angular histograms of all pixels and hotspot pixels (e.g., Fig. 4*D* and *SI Appendix*, Fig. S19) were multiplied and integrated ($n = 8$). The results were compared with a completely random distribution of hotspots. Fig. 4*E* shows that hotspots are correlated with protrusions and are not randomly distributed. An anisotropic distribution of hotspots should cause anisotropic dopamine concentration profiles. Cells could therefore shape their signal by increasing or decreasing the number of protrusions into certain directions. Obviously primary neurons are anisotropic and the release profile is also predetermined by the geometry and location of synapses. But, PC12 cells do not form classical synapses and their morphology resembles tissue cells. Such cells could use this strategy to adjust and fine-tune their chemical signaling. The distribution of hotspots around cells is most likely dependent on cell type or may even change over time for a certain cell. Such differences can be precisely investigated using our nanosensor array approach.

In summary, we present a method for spatiotemporal chemical imaging of dopamine release from cells. The spatial resolution of nanosensor arrays allows us to map hotspots of dopamine release on cell surfaces and assess anisotropy of dopamine release. We found that dopamine efflux happens more frequently at protrusions but not preferentially in regions of positive curvature such as the tips. Furthermore, we show how cell protrusions and anisotropy are correlated with dopamine release and suggest that this is a possible mechanism for cells to shape a chemical signal.

Materials and Methods

Materials and Preparation of Polymer-Wrapped Carbon Nanotubes. Chemicals were purchased from Sigma-Aldrich or IDT if not noted otherwise. To wrap SWCNTs, 2 mg of the 30-mer nucleic acid was dissolved in 1 mL of a 0.1 M NaCl solution containing 1 mg (6, 5)-enriched SWCNTs (SG65 from SouthWest Nano Technologies, distributed by Sigma-Aldrich). The solution was tip sonicated for 10 min (3-mm tip diameter, 40% amplitude, Cole Parmer) in an ice bath. Then samples were centrifuged twice for 90 min at 16,100 *g* and the supernatant was collected. All experiments were performed in PBS at pH 7.4. For solution-based experiments the stock solution was diluted to obtain a final absorption of 0.0075 at the (6, 5)-SWCNT S_{22}-peak maximum at ~570 nm.

Spectroscopy of SWCNT/Polymer Complexes. nIR-spectra were collected with a fluorescence spectrometer equipped with a 785-nm photodiode laser (450 mW), an Acton SP2500 spectrometer (Princeton Instruments), and a 1D-InGaAs OMA V detector (Princeton Experiments). For all solution-based experiments the SWCNT/nucleic acid complexes were diluted in PBS to the final concentration and 198 µl of this solution was placed in a 96-well plate. Then 2 µl of the analyte (10 mM or less) was added to yield a final concentration of 100 µM or less. All experiments were done in triplicate and repeated at least twice.

Imaging of Single SWCNTs. SWCNTs were imaged with an inverted microscope (Zeiss, AxioObserver.Z1) equipped with different objectives [Zeiss α-Plan-APOCHROMAT 100×/1.46 Oil DIC (UV) VIS-IR and Zeiss Plan-Apochromat 63×/1.40 Oil DIC] and an appropriate filter set (Dichroic 620 nm longpass, 900 nm longpass emission filter, Chroma). For image acquisition we used either a 2D OMA V InGaAs array (Princeton Instruments) with 320 × 256 pixels or a NIRvana 640 camera (Princeton Instruments) with 640 × 512 pixels. SWCNTs were excited with a 561-nm (100 mW–1 W) fiber laser (MPB VFL series). The laser was expanded by two lenses (Thorlabs) into the back focal plane of the microscope. The typical laser excitation power was 500 mW.

Cell Experiments. PC12 cells (ATCC CRL-1721.1) were purchased from American Type Culture Collection (ATCC) and cultivated according to the supplier's protocol. In short, medium consisting of F-12K medium, 12.5% horse serum, and 2.5% FBS (all from ATCC) was used. Cells attached to cell culture flasks (Corning CellBIND) and were passaged when they reached ~70% confluence. Cells were incubated at 37 °C and 5% CO_2.

Sensor surfaces were prepared by the following procedure. First, glass substrates (#1, ThermoScientific) were functionalized with (3-aminopropyl)triethoxysilane (APTES) in ethanol (1% APTES, 1% water, 1 h). Then DNA-wrapped SWCNTs [$(GA)_{15}$ ssDNA if not stated otherwise] were diluted 1:100 in PBS [corresponding to a final absorption of 0.0075 at the (6, 5)-SWCNT S_{22}-peak maximum at around 570 nm] and incubated on top of those surfaces to let them adsorb (1 h). Afterward these surfaces were rinsed 3× with PBS. Then they were incubated with a collagen solution (Collagen, Type I, C3867, Sigma) overnight at 4 °C and rinsed with PBS. For most experiments the glass substrates were mounted from the beginning in a flow chamber (ibidi sticky-Slide VI 0.4).

Finally, PC12 cells were sparsely cultivated in full medium on these surfaces to avoid clustering (at least 4 h). Cell adhesion was verified by light microscopy and the full medium was exchanged to PBS supplemented with calcium and magnesium (Sigma). Cells in the flow chamber and all buffers were kept at 37 °C before the experiment. Cell experiments were performed without an incubation chamber but given the time scale of the experiment (<10 min) the temperature was close to 37 °C. Cells were stimulated by adding 110 mM potassium chloride solution to the inlet of the flow chamber (final concentration ∼55 mM for the complete flow chamber volume).

Data Analysis and Fitting Algorithm. Movies collected during cell experiments were processed by a fitting algorithm to identify regions where sensors responded to dopamine release. During each frame, the image of 640 × 512 pixels was separated into 4 × 4-pixel groups over which mean intensity values were calculated, resulting in a time-dependent intensity trace for each of the 20,480 groups. Each intensity trace was fit to the following equation:

$$I = a + b \cdot t + c \cdot t^2 + x \cdot e^{\left(\left(-(t-y)^2\right)/2z^2\right)}.$$

The functions formed by parameters *a*, *b*, and *c* represent the possible drift in baseline intensity caused by defocusing of the microscope during the experiment. The parameters *x*, *y*, and *z* represent the amplitude, peak center, and SD, respectively, of a Gaussian function used to fit a region of sensor response. A script was used to process the movies and perform the fittings. The fitting procedure provided images of fitting parameters.

The curvature of the cell contour was calculated by using a three-point approximation (48). For each pixel of the contour the mean (curvature) of the local pixel curvature plus three adjacent pixels was calculated.

ACKNOWLEDGMENTS. We thank Klaus Schulten and Markita Landry for input and support. S.K. was supported by the Deutsche Forschungsgemeinschaft and a Liebig Fellowship (Fonds der chemischen Industrie). D.P.S. is grateful for a National Science Foundation (NSF) Graduate Research Fellowship under Grant 2388357. L.V. was supported by NSF Grant PHY1430124 and NIH Grant 9P41GM104601. The authors acknowledge the NSF-funded Extreme Science and Engineering Discovery Environment CA93S028, the Taub computing cluster (University of Illinois), and the Texas Advanced Computing Center for computational resources. Additional funding was provided by the McGovern Institute Neurotechnology Program.

1. Hyman SE (2005) Neurotransmitters. *Curr Biol* 15(5):R154–R158.
2. Thurley K, Gerecht D, Friedmann E, Höfer T (2015) Three-dimensional gradients of cytokine signaling between T cells. *PLOS Comput Biol* 11(4):e1004206.
3. Camilli A, Bassler BL (2006) Bacterial small-molecule signaling pathways. *Science* 311(5764):1113–1116.
4. Hafez I, et al. (2005) Electrochemical imaging of fusion pore openings by electrochemical detector arrays. *Proc Natl Acad Sci USA* 102(39):13879–13884.
5. Wang J, Trouillon R, Lin Y, Svensson MI, Ewing AG (2013) Individually addressable thin-film ultramicroelectrode array for spatial measurements of single vesicle release. *Anal Chem* 85(11):5600–5608.
6. Wang J, Ewing AG (2014) Simultaneous study of subcellular exocytosis with individually addressable multiple microelectrodes. *Analyst (Lond)* 139(13):3290–3295.
7. Kruss S, et al. (2013) Carbon nanotubes as optical biomedical sensors. *Adv Drug Deliv Rev* 65(15):1933–1950.
8. Polo E, Kruss S (2016) Nanosensors for neurotransmitters. *Anal Bioanal Chem* 408(11): 2727–2741.
9. Zhang J, et al. (2011) Single molecule detection of nitric oxide enabled by d(AT)15 DNA adsorbed to near infrared fluorescent single-walled carbon nanotubes. *J Am Chem Soc* 133(3):567–581.
10. Reuel NF, et al. (2013) Emergent properties of nanosensor arrays: Applications for monitoring IgG affinity distributions, weakly affined hypermannosylation, and colony selection for biomanufacturing. *ACS Nano* 7(9):7472–7482.
11. Zhang J, et al. (2014) A rapid, direct, quantitative, and label-free detector of cardiac biomarker troponin T using near-infrared fluorescent single-walled carbon nanotube sensors. *Adv Healthc Mater* 3(3):412–423.
12. Salem DP, et al. (2016) Chirality dependent corona phase molecular recognition of DNA-wrapped carbon nanotubes. *Carbon* 97:147–153.
13. Kruss S, et al. (2014) Neurotransmitter detection using corona phase molecular recognition on fluorescent single-walled carbon nanotube sensors. *J Am Chem Soc* 136(2):713–724.
14. Cragg SJ, Rice ME (2004) DAncing past the DAT at a DA synapse. *Trends Neurosci* 27(5):270–277.
15. Wise RA (2004) Dopamine, learning and motivation. *Nat Rev Neurosci* 5(6):483–494.
16. Hires SA, Zhu Y, Tsien RY (2008) Optical measurement of synaptic glutamate spillover and reuptake by linker optimized glutamate-sensitive fluorescent reporters. *Proc Natl Acad Sci USA* 105(11):4411–4416.
17. Garris PA, Ciolkowski EL, Pastore P, Wightman RM (1994) Efflux of dopamine from the synaptic cleft in the nucleus accumbens of the rat brain. *J Neurosci* 14(10): 6084–6093.
18. Liang R, Broussard GJ, Tian L (2015) Imaging chemical neurotransmission with genetically encoded fluorescent sensors. *ACS Chem Neurosci* 6(1):84–93.
19. Masharina A, Reymond L, Maurel D, Umezawa K, Johnsson K (2012) A fluorescent sensor for GABA and synthetic GABA(B) receptor ligands. *J Am Chem Soc* 134(46):19026–19034.
20. Bucher ES, Wightman RM (2015) Electrochemical analysis of neurotransmitters. *Annu Rev Anal Chem (Palo Alto, Calif)* 8(1):239–261.
21. Adams KL, Puchades M, Ewing AG (2008) In vitro electrochemistry of biological systems. *Annu Rev Anal Chem (Palo Alto, Calif)* 1:329.
22. Omiatek DM, Cans AS, Heien ML, Ewing AG (2010) Analytical approaches to investigate transmitter content and release from single secretory vesicles. *Anal Bioanal Chem* 397(8):3269–3279.
23. Keighron JD, Ewing AG, Cans AS (2012) Analytical tools to monitor exocytosis: A focus on new fluorescent probes and methods. *Analyst (Lond)* 137(8):1755–1763.
24. Gubernator NG, et al. (2009) Fluorescent false neurotransmitters visualize dopamine release from individual presynaptic terminals. *Science* 324(5933):1441–1444.
25. Zhang J, et al. (2013) Molecular recognition using corona phase complexes made of synthetic polymers adsorbed on carbon nanotubes. *Nat Nanotechnol* 8(12):959–968.
26. Bisker G, et al. (2016) Protein-targeted corona phase molecular recognition. *Nat Commun* 7:10241.
27. Bisker G, et al. (2015) A mathematical formulation and solution of the CoPhMoRe inverse problem for helically wrapping polymer corona phases on cylindrical substrates. *J Phys Chem C* 119(24):13876–13886.
28. Polo E, Kruss S (2016) Impact of redox-active molecules on the fluorescence of polymer-wrapped carbon nanotubes. *J Phys Chem C* 120(5):3061–3070.
29. Kruss S, Srot V, van Aken PA, Spatz JP (2012) Au-Ag hybrid nanoparticle patterns of tunable size and density on glass and polymeric supports. *Langmuir* 28(2):1562–1568.
30. Kruss S, et al. (2013) Adhesion maturation of neutrophils on nanoscopically presented platelet glycoprotein Ibα. *ACS Nano* 7(11):9984–9996.
31. Kruss S, et al. (2010) Stimulation of cell adhesion at nanostructured teflon interfaces. *Adv Mater* 22(48):5499–5506.
32. Greene LA, Tischler AS (1976) Establishment of a noradrenergic clonal line of rat adrenal pheochromocytoma cells which respond to nerve growth factor. *Proc Natl Acad Sci USA* 73(7):2424–2428.
33. Westerink RH, Ewing AG (2008) The PC12 cell as model for neurosecretion. *Acta Physiol (Oxf)* 192(2):273–285.
34. Attiah DG, Kopher RA, Desai TA (2003) Characterization of PC12 cell proliferation and differentiation-stimulated by ECM adhesion proteins and neurotrophic factors. *J Mater Sci Mater Med* 14(11):1005–1009.
35. Cho Y, Borgens RB (2010) The effect of an electrically conductive carbon nanotube/collagen composite on neurite outgrowth of PC12 cells. *J Biomed Mater Res A* 95(2):510–517.
36. Leach JB, Brown XQ, Jacot JG, Dimilla PA, Wong JY (2007) Neurite outgrowth and branching of PC12 cells on very soft substrates sharply decreases below a threshold of substrate rigidity. *J Neural Eng* 4(2):26–34.
37. Sudibya HG, et al. (2009) Interfacing glycosylated carbon-nanotube-network devices with living cells to detect dynamic secretion of biomolecules. *Angew Chem Int Ed Engl* 48(15):2723–2726.
38. Rodriguez PC, et al. (2013) Fluorescent dopamine tracer resolves individual dopaminergic synapses and their activity in the brain. *Proc Natl Acad Sci USA* 110(3):870–875.
39. Byrd JC, Hadjiconstantinou M, Cavalla D (1986) Epinephrine synthesis in the PC12 pheochromocytoma cell line. *Eur J Pharmacol* 127(1-2):139–142.
40. Kumar GK, et al. (1998) Release of dopamine and norepinephrine by hypoxia from PC-12 cells. *Am J Physiol* 274(6 Pt 1):C1592–C1600.
41. Zerby SE, Ewing AG (1996) Electrochemical monitoring of individual exocytotic events from the varicosities of differentiated PC12 cells. *Brain Res* 712(1):1–10.
42. Schroeder TJ, Jankowski JA, Senyshyn J, Holz RW, Wightman RM (1994) Zones of exocytotic release on bovine adrenal medullary cells in culture. *J Biol Chem* 269(25):17215–17220.
43. Hirasawa H, Contini M, Raviola E (2015) Extrasynaptic release of GABA and dopamine by retinal dopaminergic neurons. *Phil Trans R Soc London Biol Sci* 370(1672):20140186.
44. Martens S, McMahon HT (2008) Mechanisms of membrane fusion: disparate players and common principles. *Nat Rev Mol Cell Biol* 9(7):543–556.
45. Zhao WD, et al. (2016) Hemi-fused structure mediates and controls fusion and fission in live cells. *Nature* 534(7608):548–552.
46. Becherer U, et al. (2007) Quantifying exocytosis by combination of membrane capacitance measurements and total internal reflection fluorescence microscopy in chromaffin cells. *PLoS One* 2(6):e505.
47. Amatore C, Arbault S, Lemaître F, Verchier Y (2007) Comparison of apex and bottom secretion efficiency at chromaffin cells as measured by amperometry. *Biophys Chem* 127(3):165–171.
48. Belyaev AG (1999) A note on invariant three-point curvature approximations. *RIMS* 1111:157–164.

SI Appendix

High Resolution Imaging of Cellular Dopamine Efflux Using a Fluorescent Nanosensor Array

Authors: Sebastian Kruss[1]†, Daniel Salem[1], Lela Vukovic[2,5‡], Barbara Lima[1], Emma Vander Ende[1], Edward S. Boyden[3,4] , Michael Strano[1]*

Affiliations:

[1]Department of Chemical Engineering, MIT, Cambridge.

[2] Department of Physics, University of Illinois at Urbana-Champaign.

[3] Media Lab, MIT, Cambridge.

[4] McGovern Institute for Brain Research, MIT, Cambridge.

[5] Department of Chemistry, University of Texas at El Paso.

*Correspondence to: strano@mit.edu

†Current location: Department of Chemistry, Institute of Physical Chemistry, Göttingen University & Center for Nanoscale Microscopy and Molecular Physiology of the Brain (CNMPB), Göttingen

‡ Current location: Department of Chemistry, University of Texas at El Paso

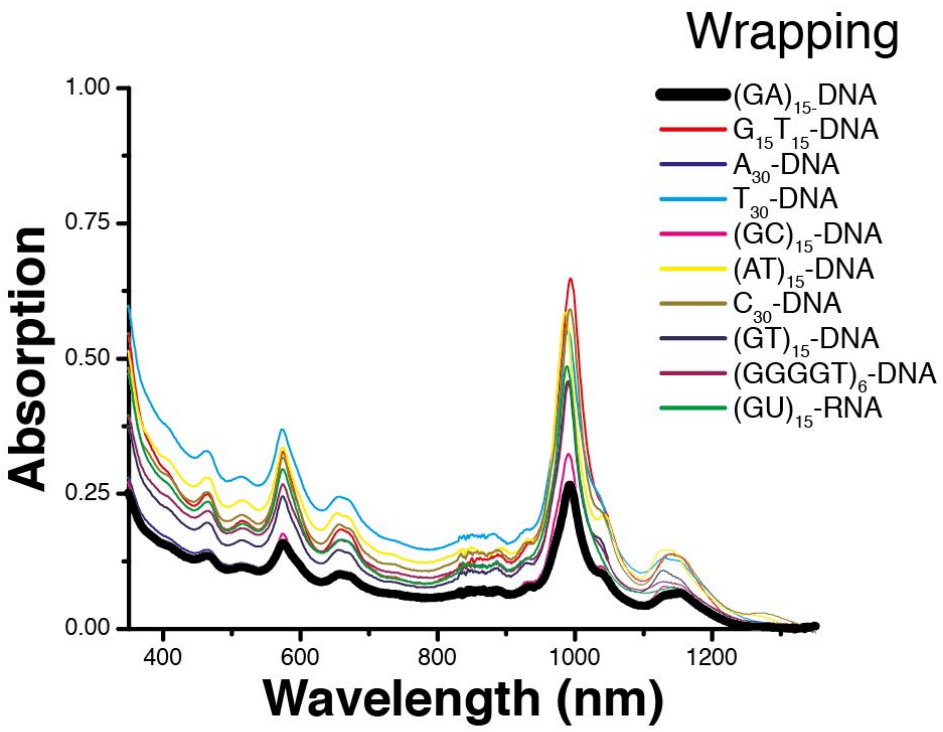

Figure S 1: Absorption spectra of nucleic acid wrapped SWCNTs used in this work. In most experiments $(GA)_{15}$-ssDNA/SWCNTs were used (spectrum is highlighted in black).

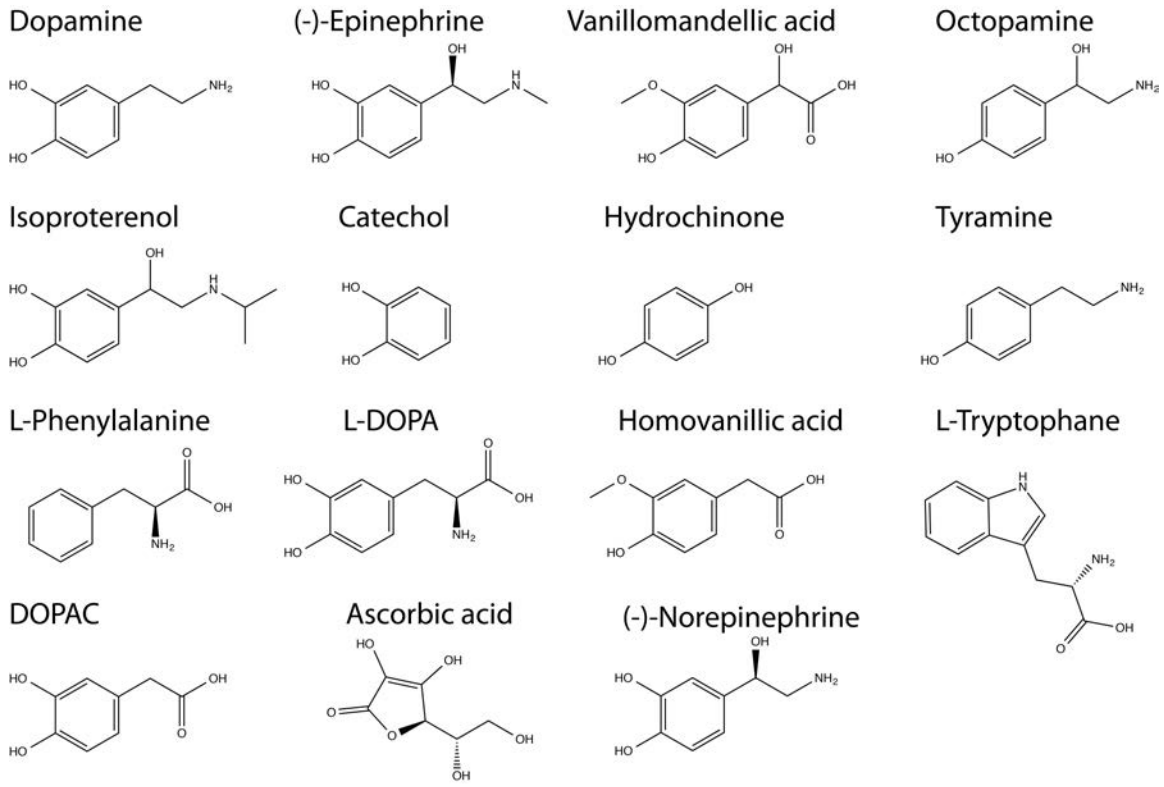

Figure S 2: Structures of tested small molecules. Note that dopamine contains three important features: Hydroxy groups, an aromatic ring and a primary amine group. We chose different important catecholamines and dopamine-related molecules to perturb the structure and identify the groups that are relevant for molecular recognition.

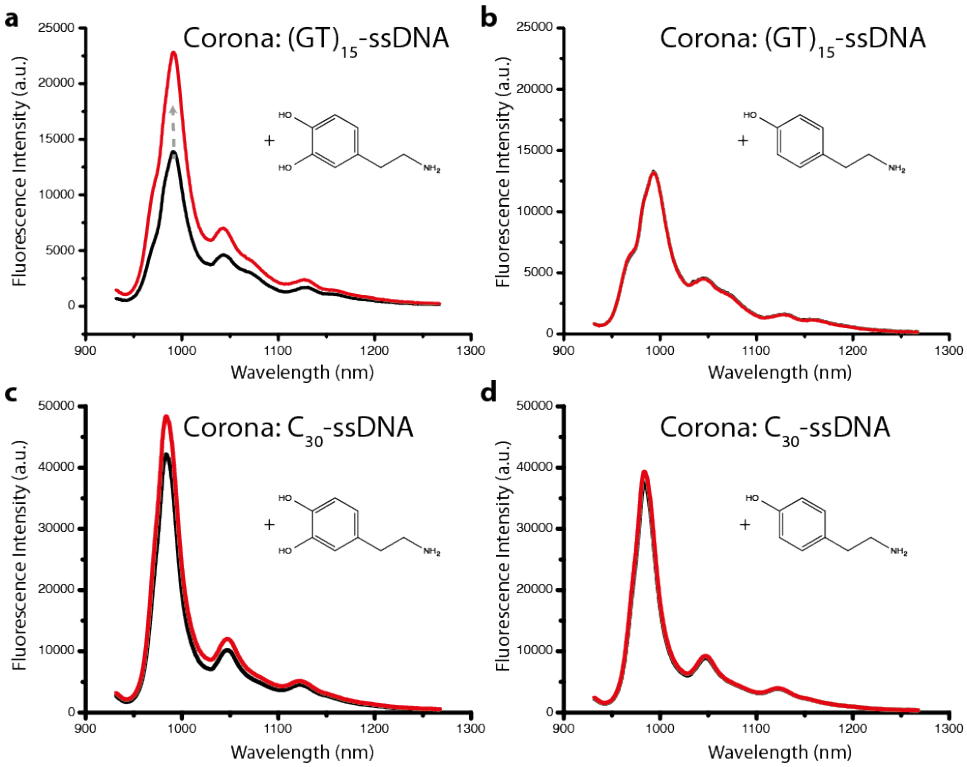

Figure S 3: The corona phase and the structure of interacting small molecules govern the near Infrared (nIR) fluorescence spectra of carbon nanotube/nucleic acid complexes: a, $(GT)_{15}$-ssDNA corona + dopamine **b**, $(GT)_{15}$-ssDNA corona + tyramine **c**, C_{30}-ssDNA corona + dopamine **d**, C_{30}-ssDNA corona + tyramine. Spectra were collected in PBS. Black: before analyte addition. Red: after addition of dopamine (10 μM in PBS). The fluorescence spectra are dominated by the peak of the (6,5)-chirality at around 990 nm. The other peaks arise from other chiralities. The spectra show that C_{30}-wrapped SWCNTs are much less responsive to dopamine. Both DNA-wrappings do not respond to tyramine (primary amine but only one hydroxy group).

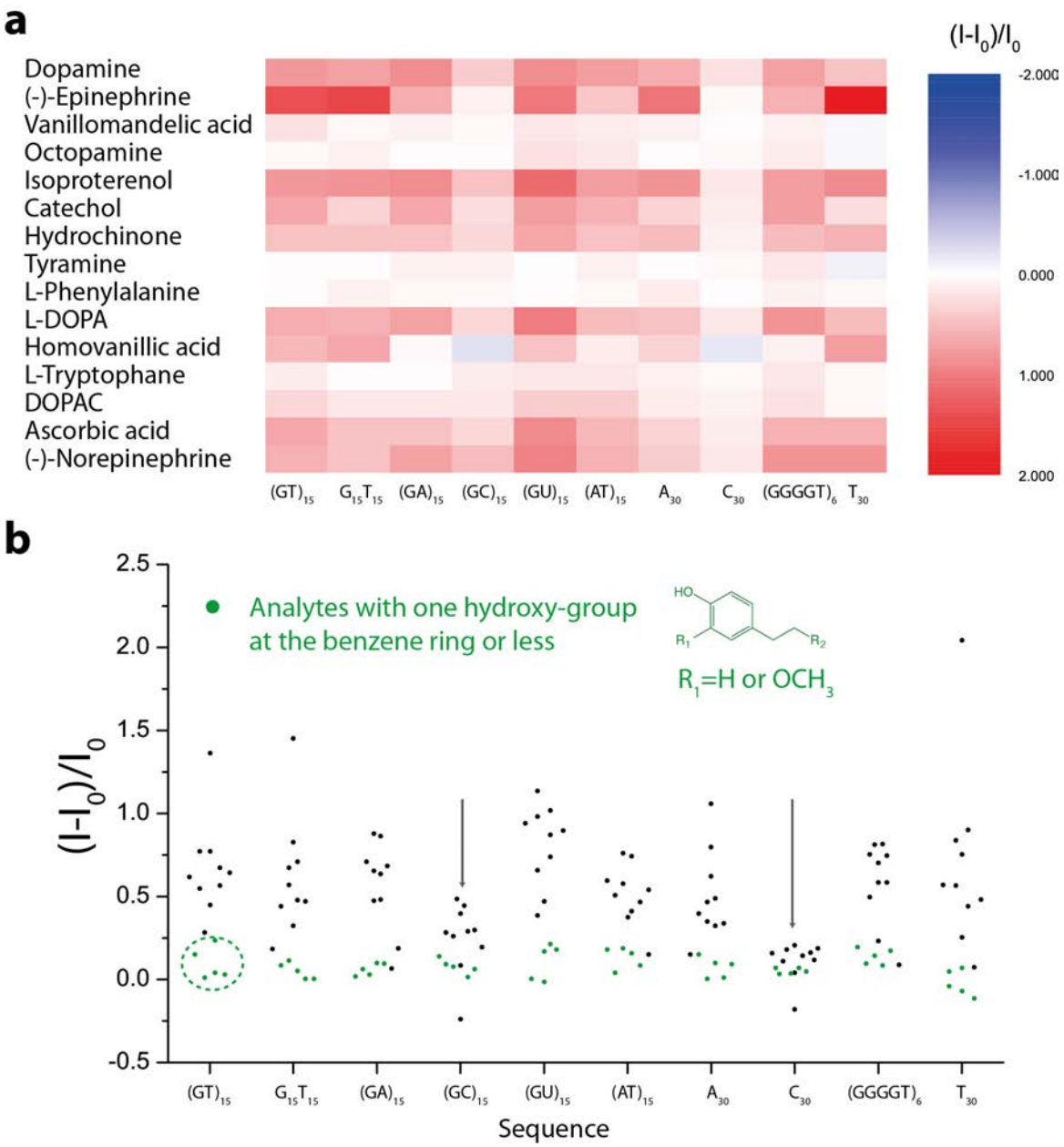

Figure S 4: Fluorescence response of DNA and RNA-wrapped SWCNTs to a library of dopamine-related small molecules. a, X-axis: Different DNA/RNA sequences. Y-axis: different molecules. **b**, Dot plot of the same data to show two major structure-function correlations: 1. Molecules with one free hydroxy group (at the benzene ring) show much smaller fluorescence changes (green dots). Molecules with two hydroxy groups (catecholamines, catechol, hydrochinone) induce much stronger fluorescence changes 2. C-containing sequences such as $(GC)_{15}$ and C_{30} create a different corona phase that renders the SWCNTs less responsive (arrows). Shown are mean values for n≥3 for all experiments. The response was defined as $(I-I_0)/I_0$, where I_0 is the fluorescence intensity at the (6,5)-SWCNT peak before and I after the addition of the analyte (100 μM).

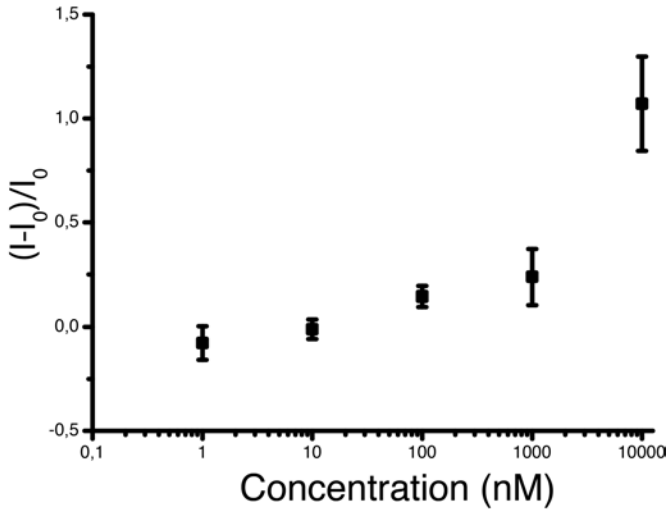

Figure S 5: ***Calibration curve of a nanosensor array response to dopamine.*** Errors are standard deviations (n ≈ 80000). The surface was incubated under cell culture conditions over night. Experiments were performed in PBS.

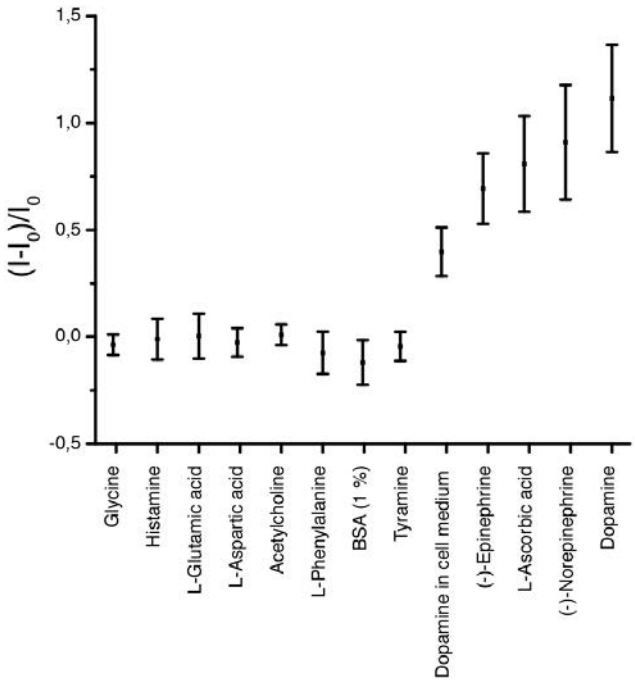

Figure S 6: Selectivity profile of a nanosensor arrays (SWCNT/$(GA)_{15}$-ssDNA) after 1 day cell culture reveals that the nanosensor array is functional under biological conditions. Errors are standard deviations ($n \approx 80000$). Analyte concentrations were 10 μM.

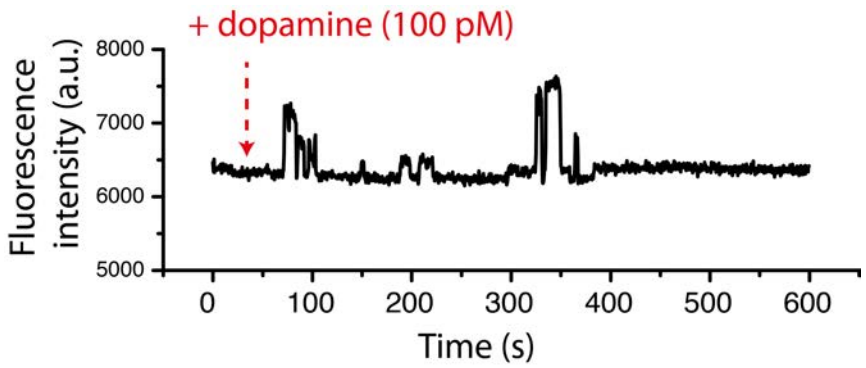

Figure S 7: Fluorescence intensity trace of a single $(GA)_{15}$-ssDNA/SWCNT in the single molecule regime (100 pM) reveals stochasticity.

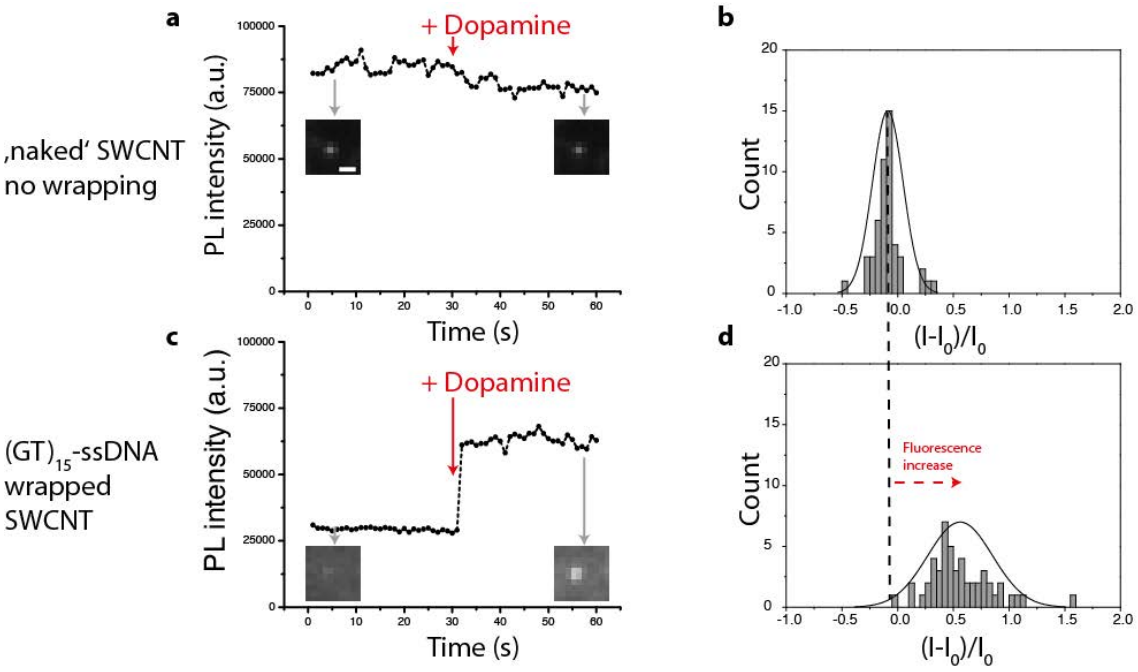

Figure S 8: Dopamine causes fluorescence increase of DNA-wrapped but not 'naked' SWCNTs. a,c Fluorescence traces (3x3 pixels) of individual SWCNTs and corresponding images before and after the addition of dopamine (100 μM in physiological PBS buffer). Scale bar = 1 μm. **a,** Naked SWCNT without polymer-wrapping . **c,** (GT)15-ssDNA wrapped SWCNT. **b,d** Histograms of SWCNT responses (normalized fluorescence change, n=50).

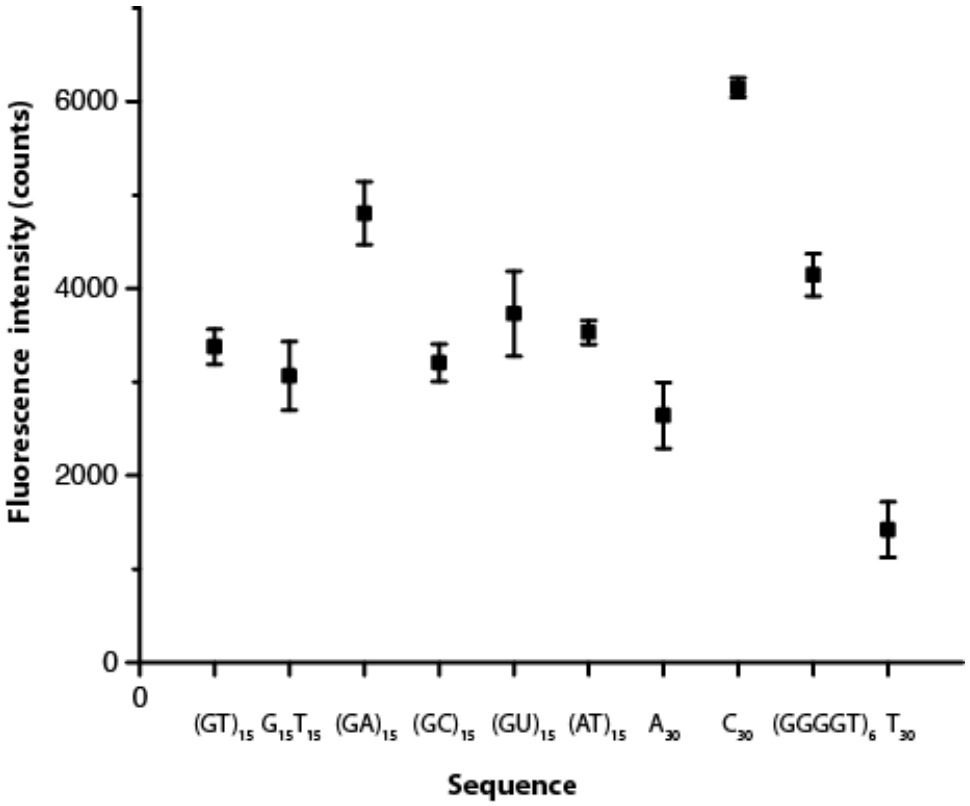

Figure S 9: Starting fluorescence intensity. Starting fluorescence intensity of different DNA-wrapped SWCNTs indicating different amounts of prequenching (in solution, PBS). Note that the DNA-sequence that responds the least to dopamine shows the highest starting fluorescence intensity (C_{30}). SWCNT/DNA concentrations were adjusted to an absorption of 0.0075 at the (6,5)-SWCNT S_{22}-peak at around 570 nm. Errors are standard deviations (n=3).

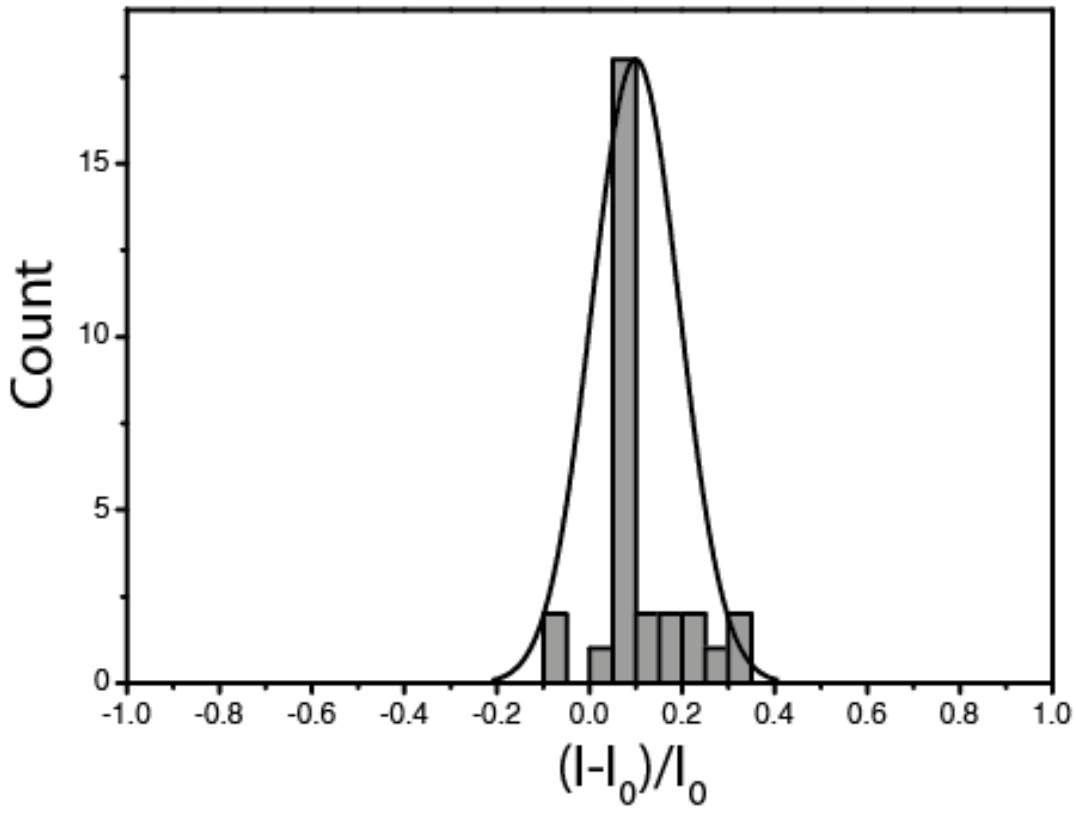

Figure S 10: 'Naked' SWCNTs do not respond to dopamine (100 μM) in PBS. Here, sodium dodecylsulfate (SDS)-wrapped SWCNTs were immobilized onto a surface and the SDS was washed away with water (1 day, 4x exchange of water). Then the fluorescence of single SWCNTs was analyzed before (I_0) and after (I) addition of dopamine. This experiments demonstrates that the polymer-wrapping is responsible for sensitivity and selectivity to dopamine.

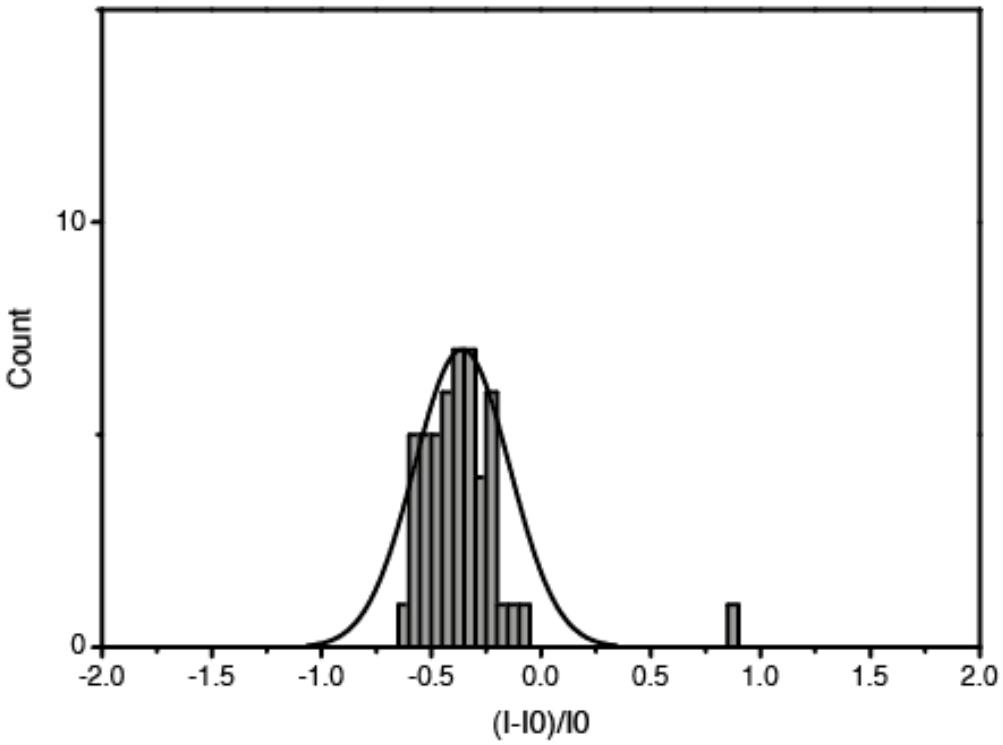

Figure S 11: Sodium dodecyl-sulfate (SDS) protects from quenching pathways and increases fluorescence (quantum yield). Here, SWCNTs that were dispersed in 2 % SDS were immobilized on glass and the aqueous 2 % SDS-solution was removed and replaced by water. This procedure reduced the SDS-concentration below the criticial micelle concentration and SDS is removed from the SWCNT surface. The fluorescence intensity of individual SWCNTs was analyzed before (I_0) and 1500 s after the washing step (I) and shows that the SDS-wrapping protects the SWCNT from quenching pathways.

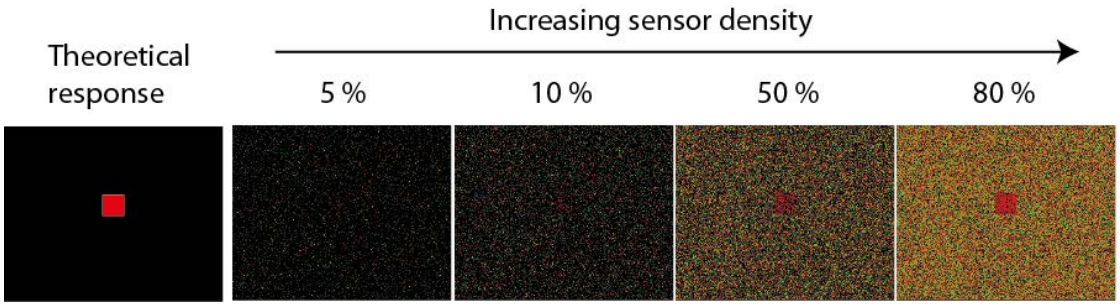

Figure S 12: Advantages of sensor arrays in low signal/noise applications. An image was created and covered with increasing numbers of sensors (pixels). Suppose that sensors can either get brighter (red) or get less bright (green) similar to the dopamine-induced increase of fluorescence in our sensors. If we assume that only the rectangular region contains the analyte only pixels (sensors) in this region should always turn red. Additionally, the turn on is assumed to be larger than for noise-related fluctuations (here we assume 30 % turn on for 'real' events). All other pixels are randomly either green or red (noise). At low sensor concentrations (5 % surface coverage) it is difficult to identify the region of interest even though all pixels in this region are red and have larger pixel values. At around 50 % surface coverage the rectangular region becomes clear. Note that the image has 320x256 pixels corresponding to around 80 000 sensors). This simulation shows that the number of sensors is critical in low signal/noise imaging applications. The spatial correlation of sensors provides a spatial filtering effect.

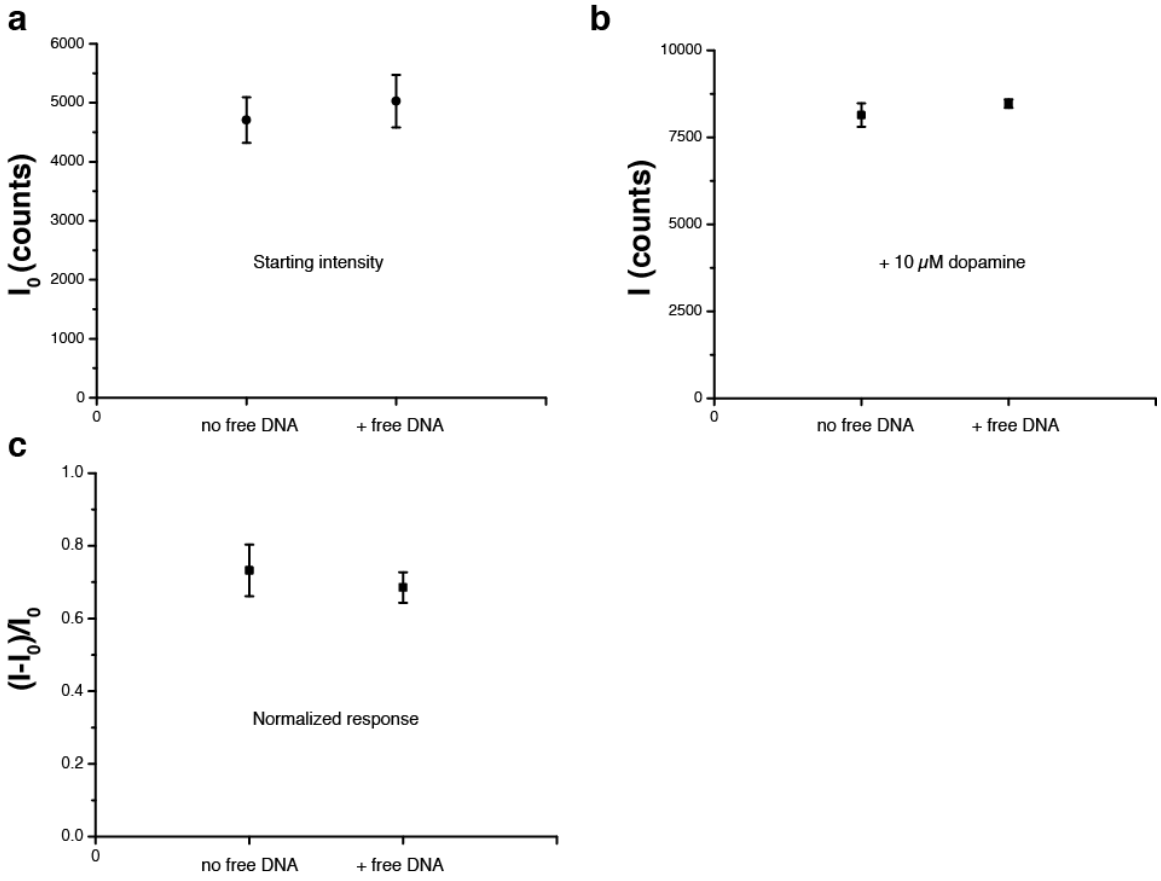

Figure S 13: Impact of free DNA on fluorescence of the sensor layer: APTES functionalized surfaces were incubated with $(GA)_{15}$-ssDNA COMOCAT SWCNTs for 1h and then functionalized with collagen and finally incubated for >1h in cell culture medium. DNA free samples were prepared by removing the free DNA by centriguation in a cutoff filter. Fluorescence intensities are mean intensities of the whole fluorescence image (320x256 Pixel). Errors are standard deviations (n=2). The results show that free DNA that adsorbs on the surface around the SWCNTs does not significantly change the sensor performance.

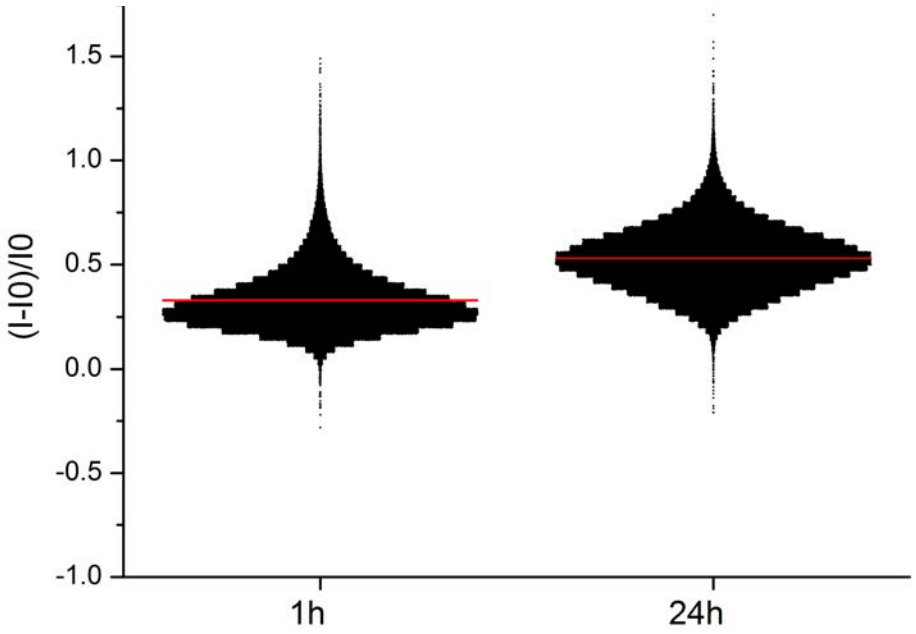

Figure S 14: Impact of SWCNT incubation period on sensor image response. (GA)15-ssDNA/SWCNT sensors were adsorbed onto a APTES-coated glass surface for different time periods (1 h vs 24 h) and coated with collagen. Then, the response to 10 μM dopamine (in PBS) was tested. The results indicate that a longer adsorption period increases the performance. This might be related to the number of SWCNTs that adsorbed during this time period.

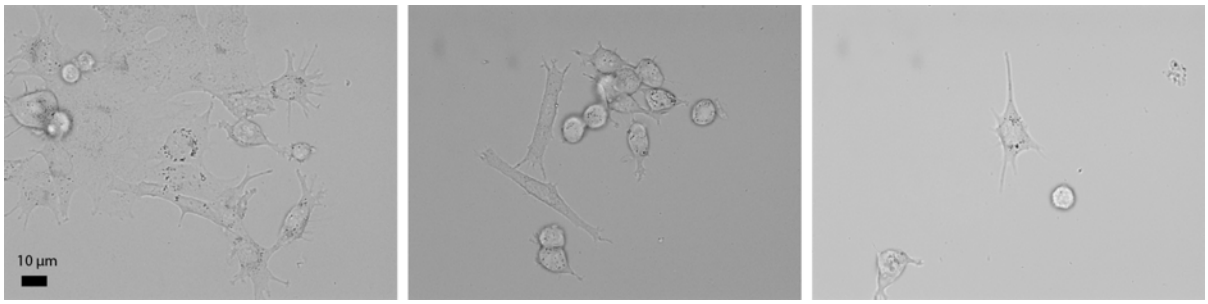

Figure S 15: PC12 cells on a nanosensor/collagen coated surface after 24 h incubation. Cells tend to form clusters and aggregate but there are also isolated cells. Some cells are adhering and form protrusions while others are round.

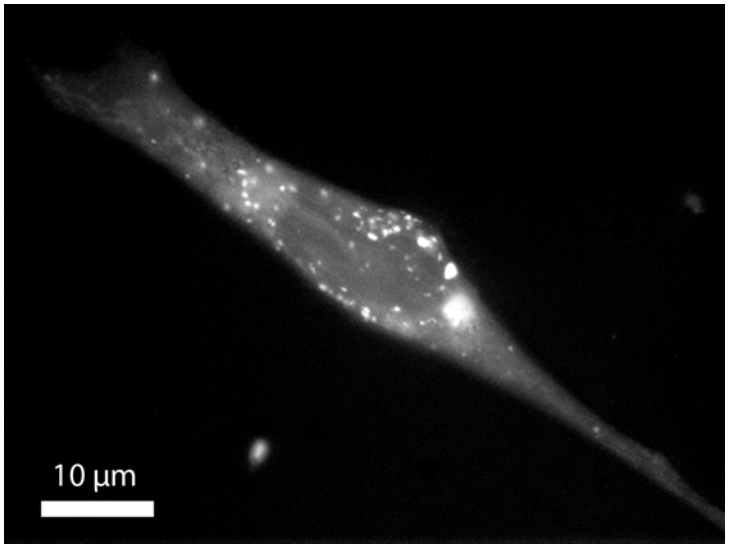

Figure S 16: Staining with false fluorescent neurotransmitters (FFNs). The image reveals that PC12 cells contain vesicles that take up dopamine homologues (FFN551) indicating that they would contain vesicles filled with dopamine.

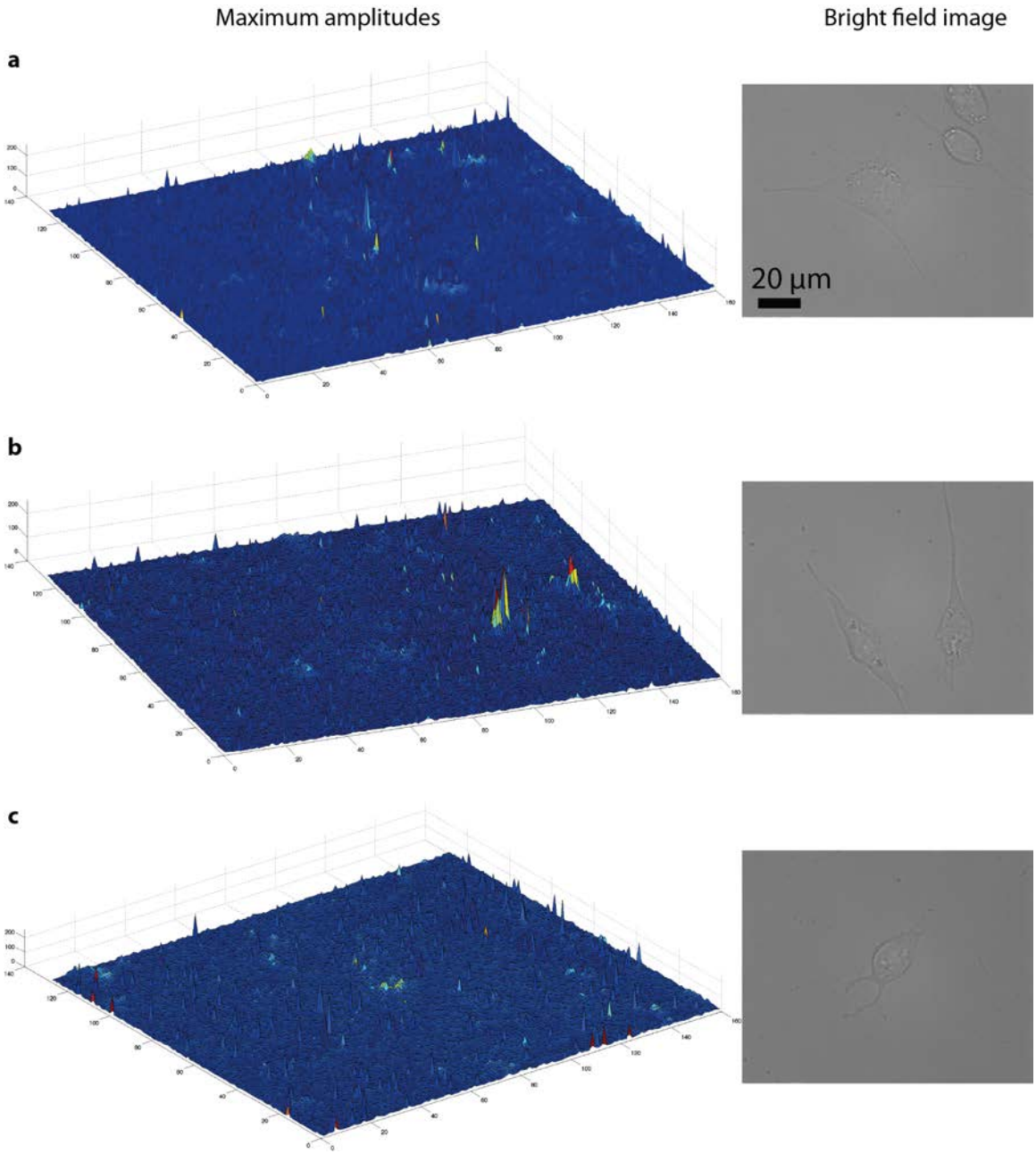

Figure S 17: Full response plots of maximal amplitudes. The plots show the maximum sensor responses (i.e. the maximum amplitude for every pixel trace such as the one shown in figure 1d). On the right there are the corresponding bright field images of cells. Note that these 3D plots represent the convoluted concentration of dopamine (due to diffusion and sensor kinetics). Therefore, also sensors outside the cell might turn on and there are typically other cells around that also release dopamine, which can affect pixels close to the border.

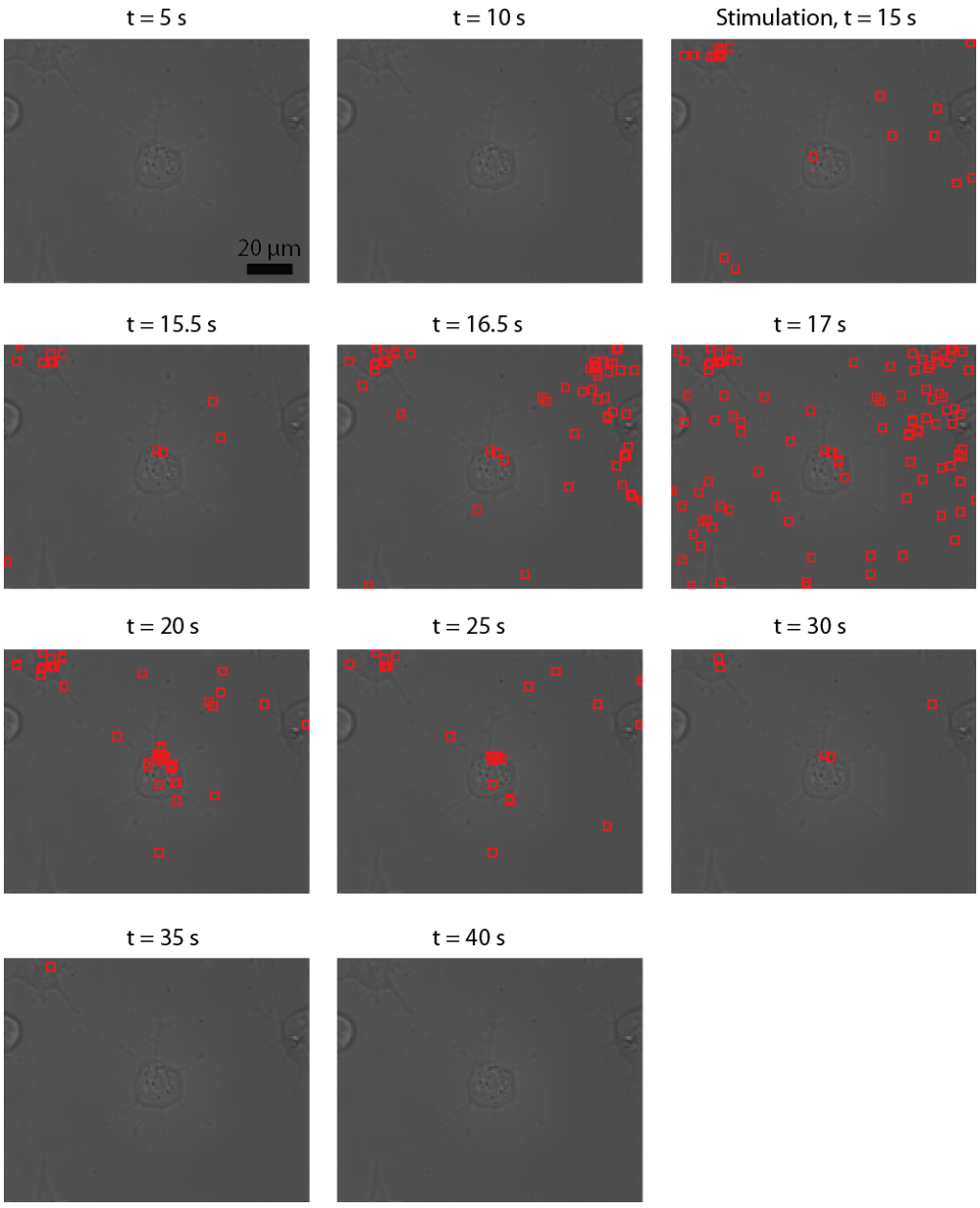

Figure S 18: Time-resolved hotspot analysis. Brightfield images of PC12 cells cultivated on nanosensor arrays. The red squares show pixels/sensors that changed their fluorescence substantially and we defined them as hot spots (>3 times mean sensor change). Hot spots are located on the cell border, under the cell and outside the cell (from released dopamine). They appear after stimulation (around t=15 s) and disappear after dopamine diffused away. Shortly after stimulation the maximum number of hot spots is reached because many sensors encountered dopamine molecules. The turn-off rates of the sensors are slower than the turn-on rates. Additionally, the frame rate of 100 ms causes a convolution of the concentration profile and sensor kinetics and therefore we do not see a dopamine wave but a snapshot of dopamine concentration changes.

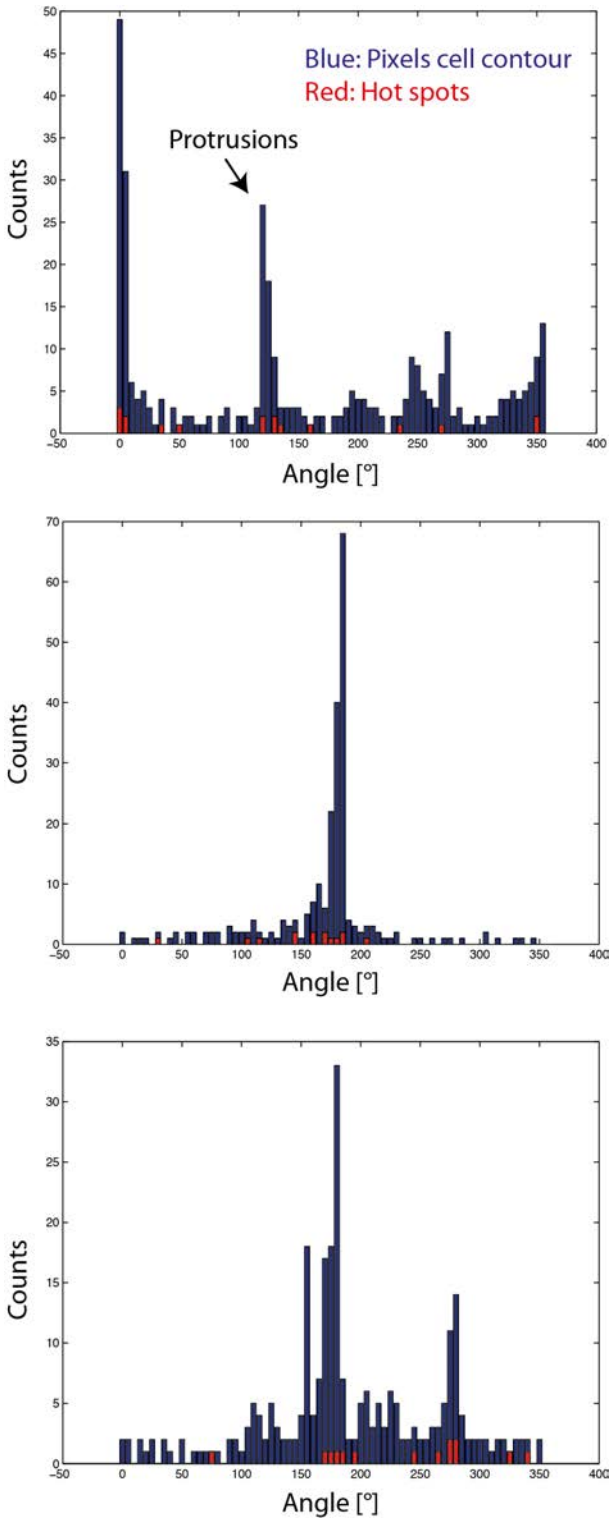

Figure S 19: Correlation between protrusions and hot spots. Histograms of angles of three independent cells show the cell contour pixels (blue) and the hotspots (red). Maxima indicate protrusions because at the angle of a protrusion the contour is elongated and there are more pixels. The plots show that protrusions and hot spots are correlated (see also figure 4 for statistics).

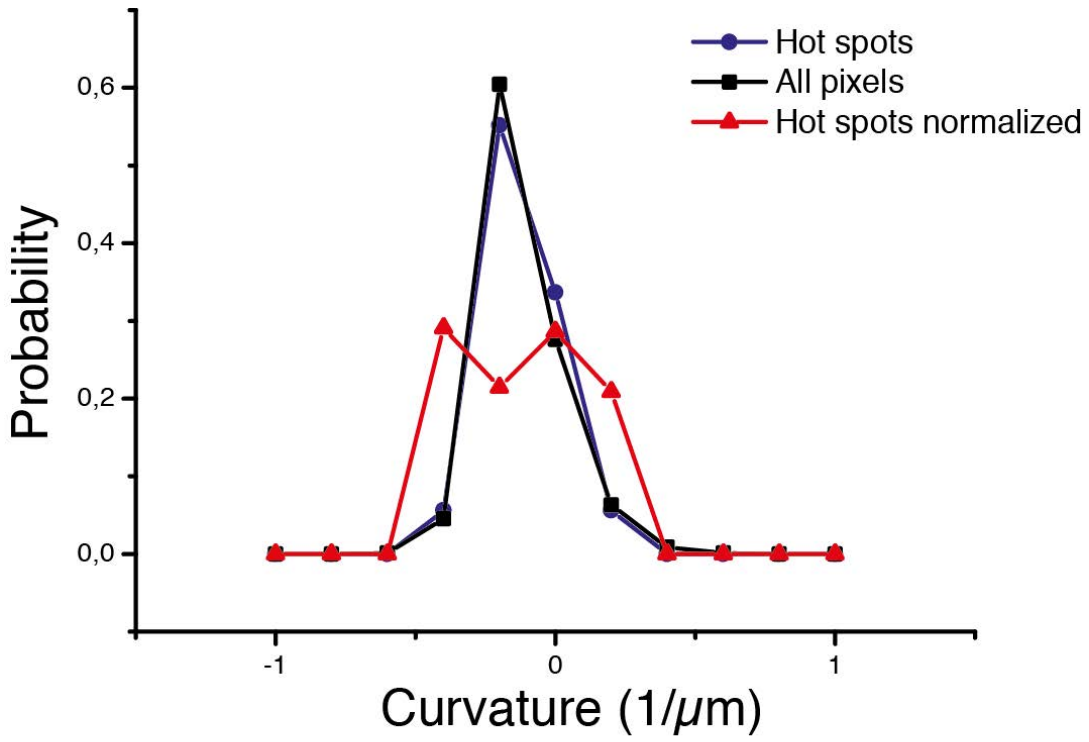

Figure S 20: Distribution of hot spots as a function of curvature. The black curve shows all pixel curvatures from n=8 cells. The blue curve shows only the hotspots. The red curve shows hot spots normalized to the relative number of pixels of this curvature (blue curve divided/normalized by the black curve). This plot was created from single cell data and especially for larger absolute curvatures there are only a few or even single data points available. Therefore, binning might have an influence on the shape of the normalized red curve. However, cells are very different in morphology and therefore single-cell representations such as in figure 4 provide more insights.

Molecular Dynamics Simulations

Interactions of SWCNTs wrapped with single stranded DNA and neurotransmitter molecules dopamine, tyramine, or catechol were examined in all-atom molecular dynamics (MD) simulations. DNA strands on SWCNTs were equilibrated in the first set of simulations. Then, neurotransmitter molecules were equilibrated with DNA-wrapped SWCNTs in the second set of simulations.

(8,8) CNTs of length l = 73 Å, built with VMD plugin Carbon Nanostructure Builder [1], were used in all the simulations. Single stranded DNA-$(GT)_{15}$, DNA-$(GA)_{15}$, and DNA-C_{30} were prepared in helical conformations with 3DNA software [2]. For the first set of simulations, DNA strands were initially placed ≈ 15 Å away from SWCNTs, with their long axes parallel to SWCNT axes. Na^+ counterions that neutralized DNA charges were placed with a VMD plugin *cionize* at potential energy minima of the prepared systems. The neutralized SWCNT-DNA systems were solvated in TIP3P water and 0.05 M NaCl, with *solvate* and *ionize* VMD plugins [1].

To examine neurotransmitter interactions with DNA-wrapped SWCNTs, we added 10 neurotransmitter molecules in random positions to SWCNT-DNA complexes, previously equilibrated for 100-150 ns. 10 neurotransmitter molecules were added per unit cell in order to collect a large number of configurations for subsequent statistical analyses of neurotransmitter binding modes. The prepared systems of neurotransmitter molecules and DNA-wrapped SWCNTs were solvated and ionized as described above, with the NaCl concentration set to 0.2 M. Dopamine and tyramine were modeled in the +1 charge state, since 97% of dopamine amine groups were predicted to be in the protonated state at pH=7.4.

All MD simulations were performed with NAMD2.9 software [3]. The systems were described with the CHARMM27 force field [4], with SWCNT atoms described as benzene-type atoms (CA). Force field parameters for the studied neurotransmitter molecules were either assigned by analogy to the CHARMM General Force Field [5, 6] (through ParamChem server [7, 8]), when exact chemical groups were already described within the CHARMM force field), or developed using the protocols of the *Force Field Toolkit* VMD plugin [9]. Topology and parameter files for dopamine, tyramine and catechol are provided in the Supplementary Information. In all simulations, the particle-mesh Ewald (PME) method [10] was used for evaluation of long-range Coulomb interactions. The timestep was set to 2.0 fs, and long range interactions were evaluated every 1 (van der Waals) and 2 timesteps (Coulombic). After 2,000 steps of minimization, ions and water molecules were equilibrated for 2 ns around the studied systems (either SWCNTs and DNA or DNA-wrapped SWCNTs and neurotransmitter molecules), which were restrained using harmonic forces with a spring constant of 1 kcal/mol/$Å^2$. Relaxation processes for three DNA strands on SWCNTs were simulated for 100-150 ns. After adding neurotransmitter molecules to each DNA-wrapped SWCNT, the resulting solvated systems were simulated for 100-200 ns with DNA strands and neurotransmitters unrestrained, while SWCNTs remained restrained. The simulations were performed in the

NpT ensemble, at a constant temperature T= 310 K, a Langevin constant γ_{Lang} = 1.0 ps^{-1}, and at a constant pressure p= 1 bar.

To analyze effects of surroundings on the potential at the SWCNT surface, we computed potential energy maps at SWCNT surfaces for several configurations of DNA-wrapped SWCNTs binding neurotransmitter molecules. For each configuration, selected from equilibrium MD trajectories, we restrained atoms of SWCNTs (with restraint of 1.0 kcal/mol/$Å^2$) as well as atoms of DNA and neurotransmitter molecules (with restraint of 0.1 kcal/mol/$Å^2$), and simulated the restrained systems for 10 ns. We evaluated the potential energy map at the SWCNT surface by averaging electrostatic potential energy contributions and Lennard-Jones contributions from 10 ns simulations of restrained systems. Electrostatic potential energy of each SWCNT atom was computed by setting its charge to $q = -1e$ for the purpose of evaluating the electrostatic potential energy (in performed 10 ns simulations, each atom had charge $q = 0$). The potential energy of each carbon atom was evaluated with the NAMDEnergy plugin in VMD [1].

References

[1] W. Humphrey, A. Dalke, and K. Schulten. VMD: Visual molecular dynamics. J. Mol. Graph., 14:33–38, 1996.

[2] X.-J. Lu and W. K. Olson. 3DNA: A software package for the analysis, rebuilding and visualization of three-dimensional nucleic acid structures. Nucleic Acids Res., 31:5108–5121, 2003.

[3] J. C. Phillips, R. Braun, W. Wang, J. Gumbart, E. Tajkhorshid, E. Villa, C. Chipot, R. D. Skeel, L. Kale, and K. Schulten. Scalable molecular dynamics with NAMD. J. Comput. Chem., 26:1781–1802, 2005.

[4] A. D. MacKerell, D. Bashford, M. Bellott, R. L. Dunbrack, J. D. Evanseck, M. J. Field, S. Fischer, J. Gao, H. Guo, S. Ha, D. Joseph-McCarthy, L. Kuchnir, K. Kuczera, F. T. K. Lau, C. Mattos, S. Michnick, T. Ngo, D. T. Nguyen, B. Prodhom, W. E. Reiher, B. Roux, M. Schlenkrich, J. C. Smith, R. Stote, J. Straub, M. Watanabe, J. Wirkiewicz-Kuczera, D. Yin, and M. Karplus. All-atom empirical potential for molecular modeling and dynamics studies of proteins. J. Phys. Chem. B, 102:3586–3616, 1998.

[5] K. Vanommeslaeghe, E. Hatcher, C. Acharya, S. Kundu, S. Zhong, J. Shim, E. Darian, O. Guvench, P. Lopes, I. Vorobyov, and A. D. Mackerell. CHARMM general force field: A force field for drug-like molecules compatible with the CHARMM all-atom additive biological force fields. J. Comput. Chem., 31:671–690, 2010.

[6] W. Yu, X. He, K. Vanommeslaeghe, and A. D. MacKerell. Extension of the charmm general force field to sulfonyl-containing compounds and its utility in biomolecular simulations. J. Comput. Chem., 33:2451–2468, 2012.

[7] K. Vanommeslaeghe and A. D. MacKerell. Automation of the CHARMM general force field (CGenFF) I: Bond perception and atom typing. J. Chem. Inf. Model., 52:3144–3154, 2012.

[8] K. Vanommeslaeghe, E. P. Raman, and A. D. MacKerell. Automation of the CHARMM general force field (CGenFF) II: Assignment of bonded parameters and partial atomic charges. J. Chem. Inf. Model., 52:3155–3168, 2012.

[9] C. G. Mayne, J. Saam, K. Schulten, E. Tajkhorshid, and J. C. Gumbart. Rapid parame- terization of small molecules using the force field toolkit. J. Comput. Chem., 34:2757–2770, 2013.

[10] T. Darden, D. York, and L. Pedersen. Particle mesh ewald: An N · log(N) method for Ewald sums in large systems. J. Chem. Phys., 98:10089–10092, 1993.

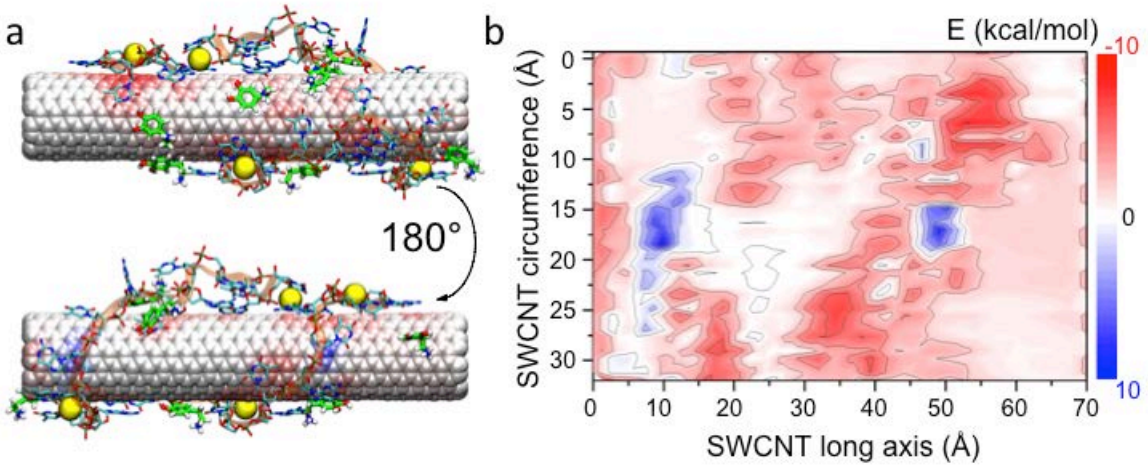

Figure S 21: Potential at the SWCNT surface due to adsorbed molecules. a, A representative snapshot of $(GT)_{15}$ DNA-wrapped SWCNT in the presence of dopamine. The SWCNT surface is colored according to the potential energy that each carbon atom experiences due to its environment. DNA and dopamine are shown in licorice representation. DNA backbone is shown as a transparent orange ribbon, and its atoms are shown in cyan (c), blue (N), red (O) and tan (P). Dopamine atoms are shown in green (C), red (O) and white (H). Stably bound sodium ions are shown as yellow spheres. **b**, Plot of the potential energy shown in (a). The range of energy values in both panels is (-10 kcal/mol, 10 kcal/mol).

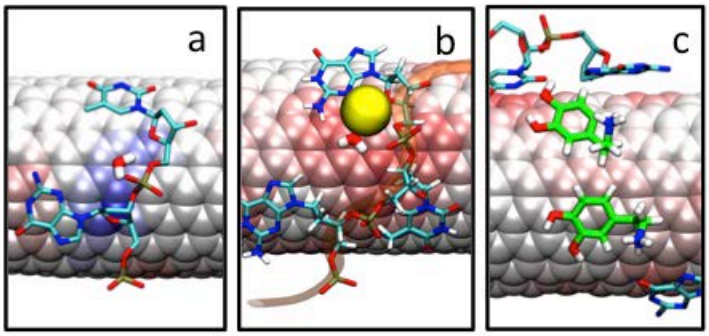

Figure S 22: Potential at the SWCNT surface due to adsorbed molecules. Magnified regions of: **a**, positive potential energy at SWCNT induced by SWCNT-adsorbed DNA backbone and sugar rings. **b**, negative potential induced by SWCNT-adsorbed DNA backbone bound to a sodium ion. **c**, slightly negative potential energy due to binding of dopamine to SWCNT. Stably bound water molecules that contribute to the potential energy at SWCNT in (a-b) are shown in licorice representation. The color scheme is the same as in Fig. S17; the range of energy values in both panels is (-10 kcal/mol, 10 kcal/mol).

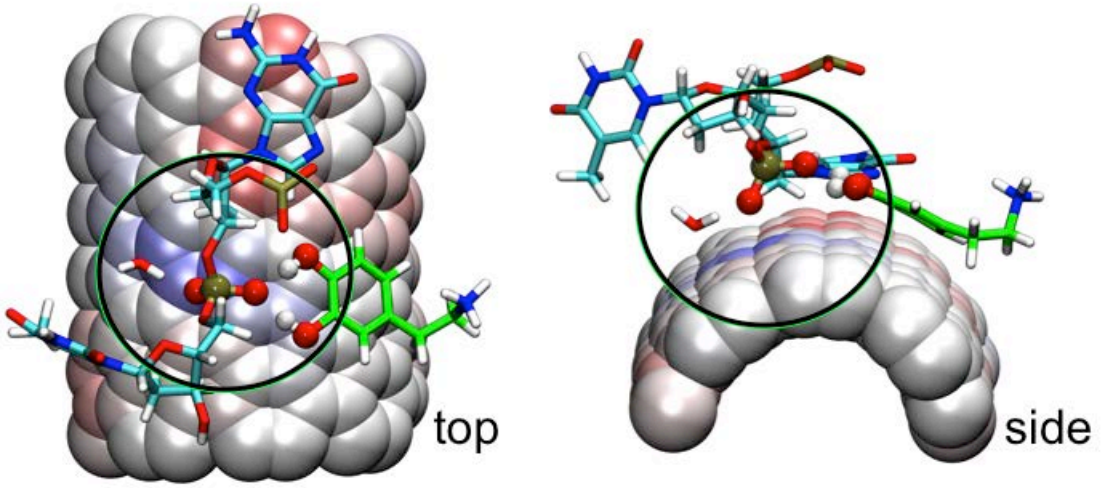

Figure S 23: Binding of dopamine can induce positive potential at the SWCNT surface. $(GT)_{15}$ DNA-wrapped SWCNT in the presence of dopamine, colored according to the potential energy value (range -8 to 8 kcal/mol). OH groups of dopamine, which pull the $–PO_4^-$ group to the SWCNT surface, are shown as spheres. A water molecule that solvates phosphate group oxygen (shown) contributes to the positive potential. The color scheme is the same as in Fig. 1.

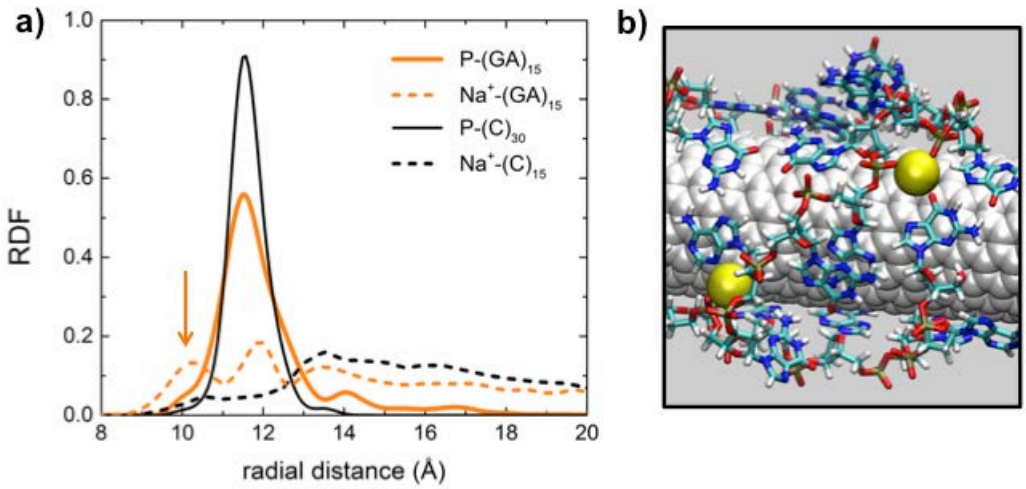

Figure S 24: a, Radial distribution of C_{30} and $(GA)_{15}$ strands (P-atoms) and their Na^+ counterions with respect to the long axis of CNT (r=0). **b**, Stacked nucleotides can form configurations that can trap Na^+ ions at the CNT surface. Sequence $(GA)_{15}$ has higher propensity than C_{30} to bind to Na^+ ions at close distance from the CNT surface (figure S20 b), thus modifying the electrostatic potential at the CNT surface.

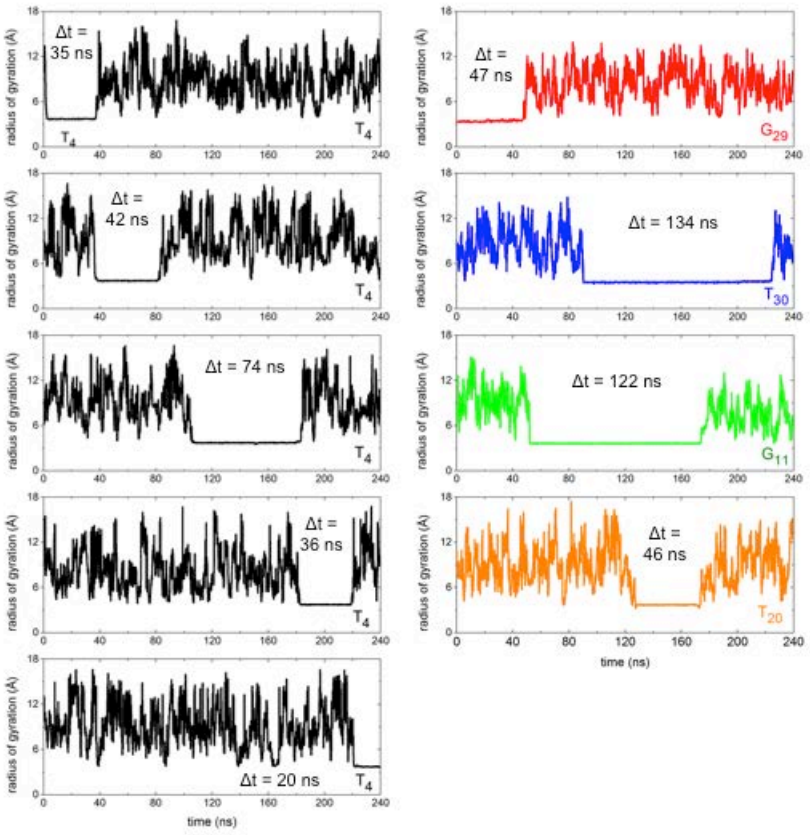

Figure S 25: Lifetimes of pockets formed from stacked DNA nucleotides and Na^+ ions. The lifetimes are obtained from tracking radii of gyration of nucleotide-Na^+ complexes, evaluated for all stable long-term complexes observed in simulations of CNT-$(GT)_{15}$ DNA with 10 dopamine molecules in 0.2 M NaCl solution. Observed lifetimes for Na^+-nucleotide binding, Δt, are recorded in each plot.

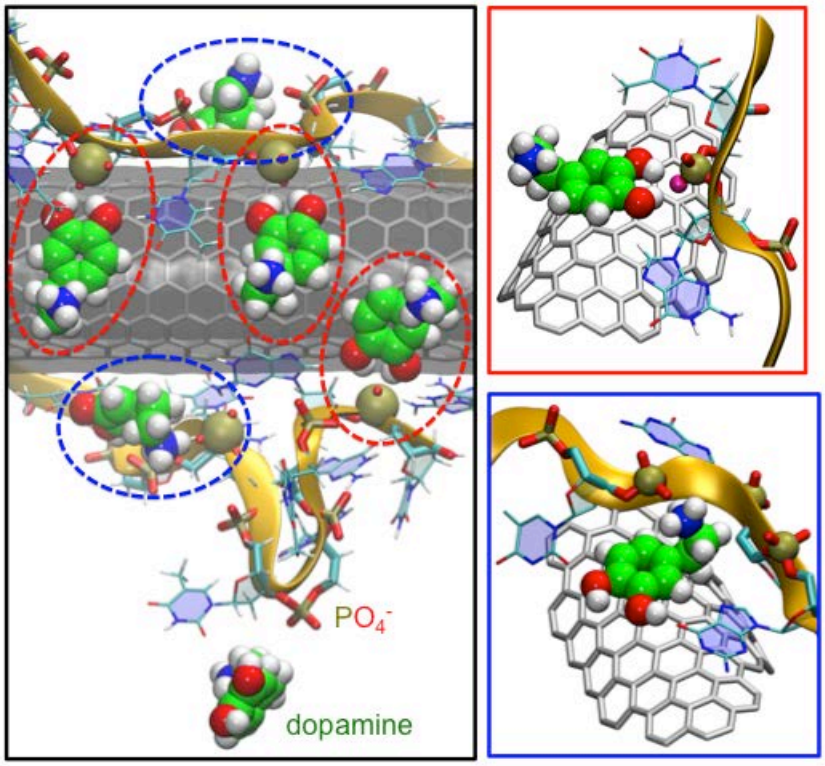

Figure S 26: Examples of binding modes of dopamine to $(GT)_{15}$ DNA-wrapped CNT. Dopamine molecules stack on the nanotube, while binding to DNA phosphate groups through hydroxyl groups (red frames), or through amine groups (blue frames). The observed binding modes lead to different electrostatic potential at the CNT surface, as shown in figure S20.